Estimation of Position and External Force of Cable Driven Surgical Robots

Mohammad H. Haghighipanah

A dissertation
submitted in partial fulfillment of the
requirements for the degree of

Doctor of Philosophy

University of Washington

2017

Reading Committee:

Blake Hannaford, Chair

Howard Jay Chizeck

Payman Arabshahi

Program Authorized to Offer Degree:
Electrical Engineering

University of Washington

Abstract

Estimation of Position and External Force of Cable Driven Surgical Robots

Mohammad H. Haghighipanah

Chair of the Supervisory Committee:
Professor Blake Hannaford
Department of Electrical Engineering

Positioning accuracy in cable driven mechanisms with motor position sensing is limited because the stiffness in these manipulators is less than rigid links. By applying Unscented Kalman Filter (UKF) and considering system dynamics in addition to motor sensing, the position estimation in these systems can be improved. To further improve the accuracy, additional observation was provided to the UKF by tracking the robot end-effector position with a camera. Furthermore, in cable driven systems the knowledge of cable's pre-tension not only improves the performance of the mechanism but can also be used as a measure to determine if the system is safe and robust to operate (e.g. too loose causes slack while too stiff causes the cable to wear and break). Thus, knowing the cable's pre-tension is important particularly in applications such as surgical robotics. To measure this initial tension, a special force gauge sensor can be used; however, these sensors are expensive and in some applications, such as surgery, it is not practical due to sterilization requirement. It is found that the stiffness parameter of cables has the highest correlation with tension. Therefore, we estimated the stiffness parameter to indirectly estimate cable's pre-tension. To estimate cable's pre-tension indirectly, first the initial tension in the cables were measured with a sensor and then the UKF was used to estimate system states and stiffness parameter simultaneously. The stiffness parameter was estimated at different tensions to find a mapping between tension and stiffness. This mapping was later used to estimate tension with UKF

without a need for force sensor. Moreover, in surgery, haptic feedback is vital for surgeons. Without haptic feedback, surgeons may exert excessive force to a healthy tissue. To address this issue, we developed a novel approach to estimate external forces acting on cable driven robots by measuring the stretch in cables caused by external force similar to Series Elastic Actuators (SEA) without actually placing an elastic element in series with the motor and load. In our approach, we took advantage of the elasticity of cables. In our method, we used two encoders to precisely measure the cable stretch. The first encoder is mounted on the shaft of the motor while the second encoder is mounted on the Joint. With the first encoder, we used robot kinematics to estimate Joint angle (q_{kin}) and with the second encoder we measured the actual Joint angle (q). Then, by subtracting these two angles we measured the stretch. Once the stretch in cables are known, either linear Hooke's law or a non-linear spring model can be used to estimate external forces.

TABLE OF CONTENTS

LIST OF FIGURES

LIST OF TABLES

ACKNOWLEDGMENTS

First, I would like express my deepest appreciation toward my great advisor Professor Blake Hannaford. His support, mentorship, depth of knowledge and kindness are exemplary and I am very grateful to have him as my Ph.D. advisor. Blake has always encouraged and inspired me with his kind and constructive comments. He has provided such a nice Ph.D. experience in his lab for me to have flexibility and freedom to be innovative and yet at the same time guided me in the right direction through his valuable inputs.

Second, I am grateful to my Ph.D. committee members, Professor Howard Chizeck, Professor Payman Arabshahi, and Professor Mehran Mesbahi for providing invaluable and helpful comments and suggestions.

I would also like to thank Professor Mohamed El-Sharkawi for his kind support and advice during my first year in the EE department. I worked as a TA for Professor El-Sharkawi during my first year. It was a pleasure to work besides him and learn from his wisdom.

I am very grateful to have such a wonderful wife, Dr. Pegah Hassanzadeh, who endlessly loved and supported me throughout my Ph.D. She has inspired me with her boundless emotional and constructive care. Furthermore, I am indebted to my great parents who has generously supported and encouraged me through every step in my life and education path. Their sacrifice and emotional support have always been great motivation for me to overcome hardships.

Finally, I would like to thank my lab mates specially Muneaki Miyasaka and Dr. Li Yangming who helped me with some of the experiments that are in this thesis. Furthermore, I would like to thank all the members of the UW BioRobics Lab including David Caballero, Danying Hu, Nava Aghdasi, Kevin Huang, and Junjie Yan for creating fun and

joyful environment to succeed.

DEDICATION

to my family.

Chapter 1

INTRODUCTION

1.1 Minimally Invasive Surgery

Minimally Invasive Surgery (MIS) is a kind of surgery in which a long thin laparoscopic instrument is used through a small incision [1]. This results in faster recovery time compared with conventional methods [2, 3]. There are a few challenges with MIS such as limited view of surgical work space, difficulties in handling of surgical tools through small incisions, lack of dexterity and haptic feedback [2–4]. These limitations can be resolved with Robotic Surgical Assistants (RSA), which are becoming more popular in MIS. Also, for more complex surgical operations such as coronary artery bypass and mitral valve repair [5–9], robotic surgery enables surgeons to achieve better results [10]. These systems are able to perform sophisticated maneuvers inside patient's body with their improved dexterity. Combining these systems with stereo-vision enables a surgeon to perform surgical tasks that are precise and effective. Moreover, hand movement with these tele-operated systems can scale down and any tremor can be filtered out [3, 11]. The medical robots provide great opportunity for surgeons to improve the precision and treatment while performing complicated surgical procedures.

Da Vinci is a robotic surgical assistant that has been developed by Intuitive Surgical, Inc. [12] Da Vinci is a master-slave tele-operated device. The master consists of control console with 3D view of the surgical work space that allows the surgeon to control two arms simultaneously by hand. The system increases the precision by allowing motion scaling. The slave side consist of several arms and 3D endoscope. Each arm has 7-DOF [12]. Though da Vinci is FDA approved and it is an excellent platform for robotic surgery, it is very expensive and not affordable for many research institutes. Raven-II®is an open source experimental

research platform cable driven robotic surgical assistant; it has two arms with 7-DOF. The first 3-DOF are dedicated for positioning and an attachable instruments can be plug to the last 4-DOF (pitch, yaw, roll, and grasping). The robot is tele-operated in a master-slave scheme using TCP or UDP protocols. Raven-II can be used for animal surgery, surgical training tasks, and other robotic surgical assistance tasks; however, it is not designed for human subjects [13]. Raven-II is similar in terms of degree of freedom and manipulation to da Vinci at much lower cost, which makes it a perfect platform for research institutes to perform research in the surgical robotics field.

1.2 Cable Driven Mechanism

Cable driven manipulators have a long history and they are found in many applications including parallel robots, wearable robots, humanoid robots, surgical robots, and haptic devices. Cable driven mechanisms consist of rigid links, cables, capstans, and pulleys. Usually a cable is multiply wrapped in a figure eight shape around input and output capstans to achieve high stiffness [14]. In these manipulators, power is transmitted through cables to move the end-effector to the desired position and actuators can be installed remotely from the driven axes. This kind of power transmission provides several advantages over non-cable driven mechanisms including lower inertia, structural simplicity, compact design, and remote actuation. Remote installation of the actuators realizes lightweight and compact design. Low inertia reduces the energy that is needed to move the link which is desirable in robot applications. In surgical robotics, compact design and low inertia are requirements and consequently many advanced surgical robots such as Da Vinci and Raven-II are cable driven systems. Also, in a fully cable driven manipulator, sensitive parts are located away from the end-effector, which is then suitable for harsh environments [15–17]. In surgical robotics this is beneficial due to sterilization requirements. However, the use of cable in robot manipulators introduces new challenges to control of the systems due to elasticity of cables and their nonlinear properties [18]. Moreover, cables transmit power thorough tension and therefore to treat them as a rigid link, the cables must remain under tension [16, 18]. Also, compared

to rigid links, the stiffness of cable is lower, which may cause undesirable vibrations [16] and a relative position error between motor and link [18]. If cable elasticity is not modeled in dynamic equations and an appropriate control compensation is not considered, the accuracy of a cable driven robot is limited.

Most medical manipulators are closed-loop servo-controlled mechanisms. Closed loop control requires the precise measurements of each joint. The most common approach is to use an optical encoder on the shaft of each motor and use deterministic forward kinematics to calculate joint position. However this method assumes the drive train is infinitely stiff and has no backlash. There are prior research on calibrating robot kinematic parameters, [19, 20] however these methods do not consider cable stretch [21]. Adding additional optical sensors directly on each joint is expensive and requires additional wiring. Moreover in surgical robots, the use of an end-effector sensor may be difficult or costly due to sterilization requirements [18]. In Raven-II, all the encoders are mounted on the motors, and joint position is calculated solely based on Motor Position Sensing (MPS). Although cable stretch errors are not generally perceptible in teleoperation, to explore automation of surgical tasks, more accurate joint position estimation is required.

1.3 Series Elastic Actuator

Conventionally, Robots are designed to have maximum transmission stiffness from actuator to loads [22]. However, "Stiffness Isn't Everything" according to [23]. Lower stiffness has several advantages such as better force control, improved shock tolerance and lower reflector inertia [23]. In Series Elastic Actuators (SEA), an elastic component, usually a spring, is connected in series between the actuator and the load. Series elasticity improves force accuracy by turning the force control problem into position control problem [24]. In these actuators, usually metallic linear springs are being used for their elastic elements and Hookes Law is used to estimate force [25]. These actuators are usually used in robotic legged locomotion applications using metal or composite springs [26–30].

1.4 State Estimation and Filtering

Generally, measurements will always contain error and they are never perfect [31]. State estimation is the process of determining the value of states from indirect observation or inaccurate sensor data. Filtering is the process of obtaining the best current estimate from noisy data [32]. In general, an optimal or best estimate from given information is desirable. The Kalman filter was created in 1960 as a tool for filtering and prediction of linear systems with Gaussian uncertainty [31]. Kalman Filter can estimate states of a system indirectly from systems that are not directly observable and it can also estimate system sates from noisy sensor data. The filter works in two steps process: prediction and update. In the prediction step, the filter calculates an estimate of the current state, and in the next step, when the next measurements are observed, the filter updates the estimate using a weighted average. Since this algorithm works recursively, it is suitable for real-time applications using only the current measurements and previously calculated states [33]. However, most physical systems are non-linear. The Extended Kalman Filter (EKF) is widely used for state estimation of non-linear systems. However, the EKF uses the Taylor series to approximately linearize the system which is a source of errors. Moreover, its linearization step requires computing the derivative of the non-linear system. For such non-linear systems, Julier et, al.[34] proposed the Unscented Kalman Filter (UKF). The UKF uses a deterministic sampling technique to compute sigma points without a need for derivatives. The mean and covariance of these sigma points describes the predicted state [35]. The UKF is simpler to implement and it is accurate to at least second order. As the non-linearity of the system increases, the UKF performs better than EKF [34].

1.5 Thesis Aims

The goal of this thesis is to improve positioning accuracy in cable driven robots and estimate cables pre-tension and external forces. To accomplish former, we propose utilizing the Unscented Kalman Filter (UKF), a set of stereo cameras, and robot dynamics to estimate

joint angles. To achieve latter, we propose to estimate cable's pre-tension by estimating the stiffness parameter and mapping the stiffness to tension. Moreover, we propose two methods to estimate external forces acting on robot. First method uses UKF and robot dynamics while the second method takes advantage of cable's elasticity to estimate external forces acting on robot. The rest of this thesis is organized as follows:

In Chapter 2, the dynamics for a rigid serial link manipulator and cable driven robot are explained. Furthermore, the way in which to solve the inverse/forward dynamics is described based on [36]. We also describe Raven-II hardware and kinematics components in this chapter. The system dynamics explained in this chapter is used throughout this dissertation.

In Chapter 3, we propose utilizing Unscented Kalman Filter and the dynamics from Chapter 2 to improve the control precision and robustness of a cable driven surgical robot, particularly for automation applications. The dual UKF (simultaneously estimating the states and system parameters) [34] was also used offline to estimate cable coupling parameters. The experimental results showed that the proposed method improved joint position estimation precision and the estimation consistency, especially on the more elastic links.

In Chapter 4, we furthered improve the positioning of cable driven manipulators by observing the end-effector with a stereo camera. We input the camera measurements into the UKF for state estimation. We used the dual UKF to estimate cable parameters and states offline and we evaluated the effectiveness of the proposed method on a Raven-II experimental surgical research platform. Furthermore, we tested the reliability of state estimation under camera occlusion. We found that when the system dynamics is tuned with offline UKF parameter estimation, the camera occlusion has no effect on the online state estimation.

In Chapter 5, first we propose a method to estimate cable pre-tension indirectly by estimating the stiffness parameter of cables. Then we proposed two methods to estimate external forces acting on the robot in all four quadrants by using cable stretch and dynamic based methods utilizing system dynamics and UKF. We assessed the effectiveness of these methods on the third link of the Raven-II. From experiments with the tension estimation

technique, it can be determined if the cable pre-tension is in the safe range. Also, both the cable stretch and UKF based methods can be used to estimate external forces on all quadrants.

This thesis includes material from the following publications:

- Haghighipanah, M., Li, Y., Miyasaka, M., & Hannaford, B. (2015, September). Improving position precision of a servo-controlled elastic cable driven surgical robot using unscented kalman filter. In Intelligent Robots and Systems (IROS), 2015 IEEE/RSJ International Conference on (pp. 2030-2036). IEEE.

- Haghighipanah, M., Miyasaka, M., Li, Y., & Hannaford, B. (2016, May). Unscented kalman filter and 3d vision to improve cable driven surgical robot joint angle estimation. In Robotics and Automation (ICRA), 2016 IEEE International Conference on (pp. 4135-4142). IEEE.

- Haghighipanah, M., Miyasaka, M., & Hannaford, B. (2017). Utilizing Elasticity of Cable Driven Surgical Robot to Estimate Cable Tension and External Force. IEEE Robotics and Automation Letters.

Chapter 2

SYSTEM DYNAMICS

2.1 Dynamics of Serial Link Manipulator

The general form of the dynamic equation of a serial manipulator can be expressed similar to [36] as:

$$\ddot{q}_l = {I_l}^{-1} \left[\Gamma - F_H \left(q_l, \dot{q}_l \right) \right] \tag{2.1}$$

$$\begin{aligned} F_H \left(q_l, \dot{q}_l \right) &= F_C \left(q_l, \dot{q}_l \right) + F_G + \text{diag} \left(sign(\dot{q}_l) \right) F_{cl} \\ &\quad + \text{diag} \left(\dot{q}_l \right) F_{vl} + J^T F_{ex} \end{aligned} \tag{2.2}$$

Where: I_l is Inertia matrix; J is Jacobian; F_C are Coriolis and centrifugal; F_G is Gravitational force; $q_l, \dot{q}_l, \ddot{q}_l$ are Joint position, velocity and acceleration, respectively; F_{cl}, F_{vl} are coulomb and viscous friction, respectively; Γ, F_{ex} are joint torque and external force, respectively.

2.2 Cable Driven Robot Dynamic

The dynamical model in section 2.1 assumes the torque is directly applied on the joints of the robot. However, in a cable driven mechanisms, the applied torques in the motors are transformed by gears and transmitted through cables to the joints. Although in real systems cables are running through several idler pulleys, we model each motor as 1) connected to a gearbox, 2) the gearbox is connected to a motor capstan and 3) power is transmitted from motor capstan to the joint via one cable with nonlinear (exponential) tension-strain relationship, as shown in Fig. 2.1. With this simplification, similar to [37, 38] the dynamics for each motor and transmission can be represented as:

$$\ddot{q}_m = (1/I_m)(\tau - \tau_m - \tau_{rn}) \tag{2.3}$$

$$\tau_m = \tau_{cm}\text{sign}(\dot{q_m}) + \tau_{vm}\dot{q_m} \tag{2.4}$$

$$\tau_{rn} = r_{mc}\gamma/N \tag{2.5}$$

$$\begin{aligned}\gamma = k_e(e^{q_{mc}r_{mc}-q_l r_l} - e^{q_l r_l - q_{mc}r_{mc}}) \\ +2b_e(\dot{q_{mc}}r_{mc} - \dot{q}_l r_l)\end{aligned} \tag{2.6}$$

$$\Gamma = r_l\gamma \tag{2.7}$$

Where: $q_m, \dot{q}_m, \ddot{q}_m$: are motor position, velocity and acceleration, respectively; k_e, b_e: are cable stiffness and damping; τ_{cm}, τ_{vm}: are motor coulomb and viscous friction; r_{mc}, r_l: are capstan radius of motor and link, respectively; N, I_m: are the gear ratio and motor inertia of the motors, respectively; τ, Γ: are torques on motor and joint, respectively.

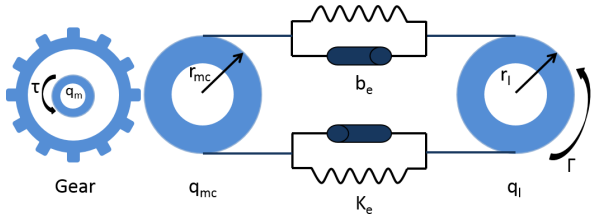

Figure 2.1: Schematic drawing of a generic cable driven system. Motor shaft is connected to a gearbox and capstan is fixed on the gearbox shaft.

2.3 Inverse/Forward Dynamics

Inverse dynamics is used to compute torque needed for a given joint motion. The inverse dynamics is computed using the Recursive Newton Euler algorithm. Forward dynamics is used to compute acceleration given an applied torque. Our implementations of forward and inverse dynamics in this thesis are based on [36]. There are three main steps to calculate the forward dynamics of the system given in (2.1).

1. Set joint acceleration to zero to calculate Coriolis, centrifugal, and gravity torques. When joint acceleration is zero, $F_H\left(q_l, \dot{q}_l\right)$ is equal to Γ.

2. Set joint velocity, gravity, and coulomb friction to zero, and set joint acceleration to u_i which is a unit basis vector with one in the i_{th} row. Then, the i_{th} column of the inertia matrix I_{l_i} is equal to the torque calculated by inverse dynamics ($I_{l_i} = \Gamma$).

3. After calculating the F_H and I_l, joint acceleration can be calculated from (2.1).

2.4 Raven Hardware and Kinematics

The generic dynamic model of (2.1) has been applied to the Raven-II experimental research platform. Raven-II has two cable driven arms with 7 DOF per arm. Its first three DOF are dedicated to translational moves and the last four dedicated to tool motion and orientation. The motors are mounted on the base of the robot and the encoders are mounted directly on the motors. The first three DOF use Maxon RE40 brushed DC motors with encoders (Avago Technologies, model number HEDM-5540, 4000 counts per revolution). All the joints have a cable run from the motor to the joint and back to the motor. Because of the motor gear ratios, mechanism kinematics, cable pulley ratios, and cable coupling, the motor angles are related to joint angles by:

$$\begin{bmatrix} q_{m_1} \\ q_{m_2} \\ q_{m_3} \end{bmatrix} = \begin{bmatrix} t_{r_1} & 0 & 0 \\ C_{01}t_{r_2} & t_{r_2} & 0 \\ C_{02}t_{r_3} & C_{12}t_{r_3} & t_{r_3} \end{bmatrix} \begin{bmatrix} q_{l_1} \\ q_{l_2} \\ q_{l_3} \end{bmatrix} \tag{2.8}$$

Where,

$$\begin{aligned} t_{r_1} &= (r_{l1}/r_{m1})N_1 \\ t_{r_2} &= (r_{l2}/r_{m2})N_2 \\ t_{r_3} &= N_3/r_{m_3} \end{aligned} \tag{2.9}$$

and $q_{l_1}, q_{l_2}, q_{l_3}$ are the joint positions for Joint 1, 2, and 3, respectively.

$r_{l1} = 63.095mm$, and $r_{l2} = 56.298mm$ are the pulley radii of link 1 and 2. $r_{m1} = r_{m2} = r_{m3} = 5.675mm$ are the pulley radii of motor capstan for link 1, 2, and 3, respectively. $N_1 =$

$N_2 = N_3 = 12.25$ is the gear box ratio for all motors. $C_{01} = 0.14545, C_{02} = 0.007797, C_{12} = 0.008077$ are the cable coupling terms of link 0 to 1, link 0 to 2 and link 1 to 2, respectively. These values were derived from the geometry of link design. These values are shown in Table 2.1.

Table 2.1: Radius of Pulleys (r_l) and Capstans (r_{mc}); Gear Box Ratio(N); Cable Coupling Parameters, and Link Mass.

$r_{mc_1} = r_{mc_2} = r_{mc_3}$	$5.675mm$
r_{l_1}	$63.095mm$
r_{l_2}	$56.298mm$
$N_1 = N_2 = N_3$	12.25
C_{01}	0.14545
C_{02}	0.007797
C_{12}	0.008077
$Link_1\ Mass$	$0.503Kg$
$Link_2\ Mass$	$0.753Kg$
$Link_3\ Mass$	$0.407Kg$

To be able to simulate a robot using Eqn. (2.1), initial inertia matrices, mass, and Center of Mass (COM) of the system links must be identified. CAD models were used to determine these parameters for the first three links of Raven-II (Fig. 2.2).

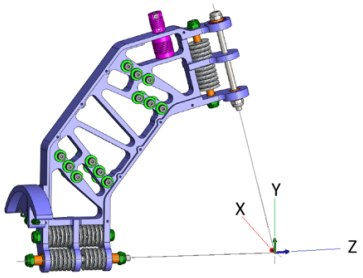

$$I_{l_1} = \begin{bmatrix} 17.376 & 0.291 & -0.374 \\ 0.291 & 11.000 & -5.483 \\ -0.374 & -5.483 & 6.499 \end{bmatrix} \times 10^{-3}\ [kg \cdot m^2]$$

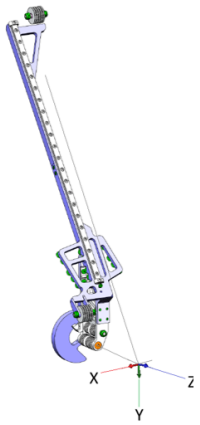

$$I_{l_2} = \begin{bmatrix} 81.579 & 0.773 & 0.762 \\ 0.773 & 44.329 & 37.973 \\ 0.762 & 37.973 & 37.686 \end{bmatrix} \times 10^{-3}\ [kg \cdot m^2]$$

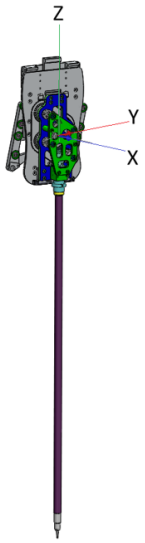

$$I_{l_3} = \begin{bmatrix} 2.908 & -0.001 & -0.066 \\ -0.001 & 3.009 & -0.009 \\ -0.066 & -0.009 & 0.355 \end{bmatrix} \times 10^{-3}\ [kg \cdot m^2]$$

Figure 2.2: CAD models of the Raven for first three joints. CAD derived mass of links 1, 2, and 3 are 0.503Kg, 0.753Kg, and 0.407Kg, respectively.

Chapter 3

IMPROVING POSITION PRECISION OF A SERVO-CONTROLLED ELASTIC CABLE DRIVEN SURGICAL ROBOT USING UNSCENTED KALMAN FILTER

3.1 Background and Literature Review

In a robot with cable driven power transmission, motors can be mounted on the base of the robot, resulting in lower mass and inertia on the arms [37]. Moreover, since motors are not mounted on the joints, these manipulators are more compact. One drawback in cable transmission is that the cables are elastic and flexible. Furthermore cable properties change over time due to cable stretch and creep (a property of cables in which they slowly lengthen under long term load). Cable dynamic properties such as stiffness and internal damping are known to vary as a function of tension [18, 38]. These changes may cause deformation which separates motor position from joint position. Furthermore in remotely mounted actuator systems, the motion of one actuator (depending on the mechanical design) may cause joint motion in another link [39]. In a cable driven robot this is called cable coupling effect. With time, variation in cable tension changes the cable coupling parameters. Furthermore, by not compensating the effect of cable coupling, a significant stress can be applied on cables which reduces the lifetime of cables. Therefore being able to estimate these parameters online can improve not only the precision of robots but also increases the lifetime of cables.

The Unscented Kalman Filter was used in [38] to estimate states and parameters of a one degree-of-freedom (DOF) cable driven test panel. It was shown that angle estimates

[1]

were robust to variation of parameters, whereas velocity estimates were not. However, state and parameter estimation of a multi-DOF serial chain robot were not investigated. In [37] the UKF state estimation on an approximate model of a multi-DOF serial chain robot was applied on a simulated Raven. In simulations the UKF provided better estimates of joint angle in the presence of cable deformation. A limitation of this work was that each link was approximately modeled as an independent link. Cable coupling and the dynamic effects of multiple links on each other was not studied. This chapter focuses on 1) Implementing the UKF in the real-time controller of an actual serial multi-DOF cable driven surgical robot and 2) estimating cable coupling parameters with the UKF to more precisely estimate joint positions. We first identify the cable coupling parameters off-line and then experimentally study whether or not increased accuracy in joint position measurement can be achieved using the UKF without joint sensors (although accurate joint sensors have been installed for validation in this study). The question were studied experimentally on the first three DOF of Raven-II. The proposed method can be applied to any cable driven mechanism with a similar cable dynamics.

3.2 Methods

3.2.1 State Estimation

The system states for Raven-II are motor angle, motor velocity, joint angle, and joint velocity for each link; the observations come from the optical encoders directly mounted on the motor shafts. Thus, the value of the joint angle needs to be estimated. We utilized the square root form of the Unscented Kalman Filter (srUKF) for state estimation [40]. The srUKF has improved numerical properties over standard UKF and it guarantees positive-semi-definiteness of the state covariance [41].

To apply srUKF the state space form of the Raven is required which can be described as:

$$\begin{aligned} \dot{\mathbf{x}} &= \mathbf{f}(\mathbf{x}, \mathbf{u}) \\ \mathbf{y} &= \mathbf{H}\mathbf{x} \end{aligned} \tag{3.1}$$

Where $\mathbf{x}$ and $\mathbf{H}$ are system states and the observation, respectively. The system states and observations for the first three links are defined as:

$$\begin{aligned} \mathbf{x}_i &:= \begin{bmatrix} q_{mi} & \dot{q}_{m_i} & q_{li} & \dot{q}_{l_i} \end{bmatrix}, i = 1, .., 3 \\ \mathbf{x} &= \begin{bmatrix} x_1 & x_2 & x_3 \end{bmatrix}^T \\ \mathbf{h_i} &:= \begin{bmatrix} 1 & 0 & 0 & 0 \end{bmatrix}, \mathbf{H} = blkdiag(\begin{bmatrix} \mathbf{h_1}, & \mathbf{h_2}, & \mathbf{h_3} \end{bmatrix}) \end{aligned} \tag{3.2}$$

Where i is the link number. The system inputs, u, are applied torques at the motors and the measurements are motor positions. The differential equation can be discretized for numerical integration using the fourth order Explicit Runga Kutta method.

The system parameters which cannot be obtained from the CAD model are: Spring constant (k_e), Damping constant (b_e), Coulomb and Viscous friction of the motor side (τ_{cm}, τ_{vm}) and the joint side (F_{cl}, F_{vl}). Furthermore, these parameters depend on cable tension. The following calculations were used to derive nominal parameter values with which to initialize the UKF parameter estimation.

These parameters are empirically approximated as shown in Table 3.1. With an external torque (τ_{ext}), dynamic model of just a motor can be represented as:

$$\ddot{q}_m I_m = \tau - \tau_{cm} sign(\dot{q}_m) - \tau_{vm}\dot{q}_m + \tau_{ext} \tag{3.3}$$

We applied a weight statically to a lever arm on the motor shaft and gradually increased it until the motor started to turn. At the time the motor starts to turn, Eqn.(3.3) becomes as follows and the Coulomb motor friction was obtained.

$$\tau_{cm} = \tau_{ext} \tag{3.4}$$

A known weight was applied to a string wound around the capstan so that motor turned at a steady state velocity ($\dot{q}_{m,ss}$). This case, Eqn.(3.3) reduces to Eqn.(3.5) and viscous friction was calculated.

$$\tau_{vm} = \frac{-\tau_{cm} sign(\dot{q}_{m,ss}) + \tau_{ext}}{\dot{q}_{m,ss}} \tag{3.5}$$

For inertia of the motor, we applied a constant input torque that could induce non-zero motor acceleration. Using τ_{cm} and τ_{vm}, the input motor torque, and the measured motor velocity and acceleration, Eqn.(3.6) yields the inertia of the motor.

$$I_m = \frac{\tau - \tau_{cm} sign(\dot{q}_m) - \tau_{vm}\dot{q}_m}{\ddot{q}_m} \tag{3.6}$$

F_{cl} is the lumped sum of the pulley and joint Coulomb friction. We experimentally measured the Coulomb frictional force of the pulley when applying average tension. We also estimated Coulomb joint friction based on the average normal force on the joint shaft and the coefficient of friction for steel on steel with lubrication. The estimated value of F_{vl} was selected to be about two orders of magnitude lower of F_{cl} [38].

The value of k_e was estimated by applying loads on a sample cable and recording the stretch. b_e is calculated from an experiment in which a load is released and the decay of subsequent oscillations in length was measured by a laser distance sensor.

Table 3.1: Unknown Parameters of the System. These parameters were empirically measured.

Symbol	Value (link 1)	Value (link 2)	Value (link 3)	Unit
F_{cl}	0.505	0.49	0.53	Nm, N
F_{vl}	0.00505	0.0049	0.0053	Nms/rad, Ns/m
k_e	720.0e3	88.0e3	9.25e3	N/m
b_e	4000.0	1380.0	400.0	Ns/m
τ_{cm}	8.11e-2	4.11e-2	5.11e-2	Nm
τ_{vm}	1.9e-4	1.8e-4	7.1e-4	Nms/rad
I_m	2.847e-4	2.847e-4	2.847e-4	kgm^2

3.2.2 Cable Coupling Parameter Estimation

To estimate cable coupling parameters the dual srUKF was used. In the dual srUKF, two separate state-space representations are used for states and parameters[42] and two parallel filter runs are made for the states and the parameters. When estimating the states the parameters are assumed to be known, and when estimating the parameters the states are assumed to be known [43]. The state space representation for state is the same as Eqn.(3.2) except that the observation of motor sensors and attached joint sensors were used offline, which makes $\mathbf{h_i}$ a 2x4 matrix. The state space representation for the parameters is given by:

$$\mathbf{w}_{k+1} = \mathbf{w}_k + \mathbf{r}_k \tag{3.7}$$

$$\mathbf{d}_k = \mathbf{G}(\mathbf{x_k}, \mathbf{w_k}) + \mathbf{e}_k \tag{3.8}$$

Where, $\mathbf{w}_k$ is the stationary process with identity state transition matrix which represents the unknown parameters, $\mathbf{G}(\mathbf{x_k}, \mathbf{w_k})$ is a nonlinear mapping that is parameterized by the vector $\mathbf{w}$. $\mathbf{r}_k$ is the process noise, $\mathbf{e}_k$ is the error, and $\mathbf{d}_k$ is the desired output from nonlinear observation on $\mathbf{w}_k$[44].

The main objective of the UKF in this chapter is to better estimate joint angles of the first three Raven axes online. srUKF was used to estimate the system states online and cable coupling parameters offline. To verify the effectiveness of the UKF in finding the true state of the joint angles, the joints were instrumented with additional optical encoders (Avago Technologies, model number AEDA-3300, 80000 counts per revolution, first two joints and linear optical encoder MicroE Systems, model number Mercury II 1600, resolution 5 μm, for the third prismatic joint) (Fig. 3.1) and their output was recorded for comparison with the estimated joint angles.

To initialize the value of its motor encoders, the robot undergoes a process known as "homeing". During "homeing", each joint rotates until it reaches physical joint limits. At this position, the encoders are initialized. Both the motor position sensors and attached joint position sensors are synchronized and initialized during homeing.

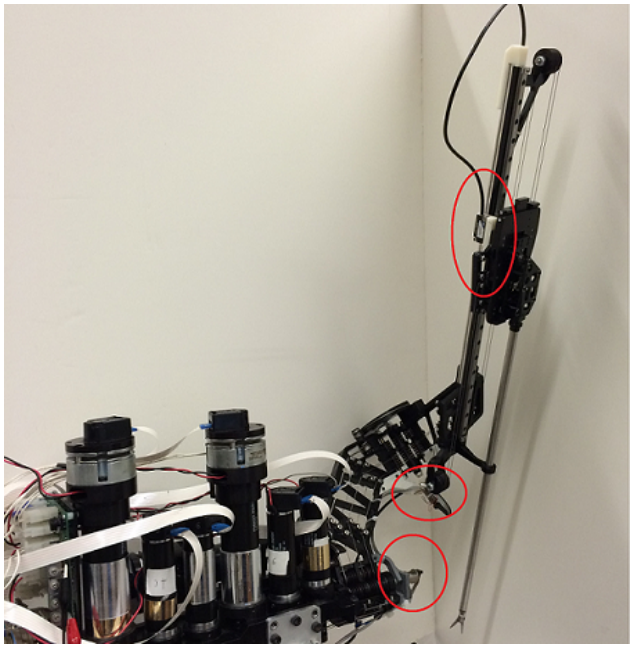

Figure 3.1: Optical incremental encoders are mounted directly on each joint to measure the actual joint position for validation. Their value was used only for validation and not used in the controller or the UKF online state estimation.

To test the cable coupling parameter estimation algorithm, a sinusoidal desired trajectory was created for each joint. A PD controller based on feedback from the motor encoder drove the motor to follow the input trajectory. Since the main objective of this chapter is to study the state estimation performance of the UKF and not the PD controller, the feedback input of the controller is the motor position, not the UKF estimated states or the joint encoders. Furthermore, accurate tracking by the PD controller is not required because the UKF is tasked with estimating actual joint trajectories.

To study the robustness of the state estimation, the UKF was tested under two different cable tensions "High" and "Low" (Table 3.2). In addition, in a real world scenario, when the robot picks up an object, the system dynamics change. To test the robustness of the system under varying loads, the robot picked up an object weighing (100 g) under High tension.

The srUKF algorithm, Raven forward/inverse dynamics, and Raven control software were implemented in C++ and communicated with each other using "topics" of the Robotic Operating System (ROS)[45] for real time communications. From the Raven control software, a node called "r2control" publishes states of the robot in real time through a topic called "ravenstates", and the UKF subscribes to the same topic to receive joint states and torques. The computer running the square root UKF is Linux ubuntu 12.10 64-bit system with Intel Core i5-3330 processor and 8GB of RAM.

3.3 Square Root Unscented Kalman Filter

The srUKF is described in [40] as:

Initialize with:

$$\hat{\mathbf{x}}_0 = \mathbb{E}[\mathbf{x}] \quad \mathbf{S}_0 = \text{chol}\{\mathbb{E}[(\mathbf{x_0} - \hat{\mathbf{x}}_\mathbf{0})(\mathbf{x_0} - \hat{\mathbf{x}}_\mathbf{0})^T]\} \tag{3.9}$$

$$\text{For} \qquad k \in 1, ..., \infty \tag{3.10}$$

Sigma point calculation and time update:

$$\chi_{k-1} = [\hat{\mathbf{x}}_{k-1} \qquad \hat{\mathbf{x}}_{k-1} + \gamma \mathbf{S}_k \qquad \hat{\mathbf{x}}_{k-1} - \gamma \mathbf{S}_k] \tag{3.11}$$

$$\chi^*_{k|k-1} = \mathbf{F}[\chi_{k-1}, \mathbf{u}_{k-1}] \tag{3.12}$$

$$\hat{\mathbf{x}}^-_k = \sum_{i=0}^{2L} \mathbf{W}^{(m)}_i \chi^*_{i,k|k-1} \tag{3.13}$$

$$\mathbf{S}^-_K = \text{qr}\{[\sqrt{W^{(c)}_1}\chi^*_{1:2L,k|k-1} - \hat{\mathbf{x}}^-_k) \quad \sqrt{\mathbf{R^v}}]\} \tag{3.14}$$

$$\mathbf{S}^-_K = \text{cholupdate}\{\mathbf{S}^-_K \quad , \quad \chi^*_{0,k} - \hat{\mathbf{x}}^-_k \quad , \quad W^{(c)}_0\} \tag{3.15}$$

$$\chi_{k|k-1} = [\hat{\mathbf{x}}^-_k \qquad \hat{\mathbf{x}}^-_k + \gamma \mathbf{S}^-_k \qquad \hat{\mathbf{x}}^-_k - \gamma \mathbf{S}^-_k] \tag{3.16}$$

$$\mathbf{y}_{k|k-1} = \mathbf{H}[\chi_{k|k-1}] \tag{3.17}$$

$$\hat{\mathbf{y}}^-_k = \sum_{i=0}^{2L} \mathbf{W}^{(m)}_i \mathbf{y}_{i,k|k-1} \tag{3.18}$$

Measurement update equations:

$$\mathbf{S}_{\tilde{\mathbf{y}}k} = \text{qr}\{[\sqrt{W_1^{(c)}}[\mathbf{y}_{1:2L,k} - \hat{\mathbf{y}}_k] \quad \sqrt{\mathbf{R_k^n}}]\} \tag{3.19}$$

$$\mathbf{S}_{\tilde{\mathbf{y}}k} = \text{cholupdate}\{\mathbf{S}_{\tilde{\mathbf{y}}k} \quad , \quad \mathbf{y}_{0,k} - \hat{\mathbf{y}}_k \quad , \quad W_0^{(c)}\} \tag{3.20}$$

$$\mathbf{P_{x_k y_k}} = \sum_{i=0}^{2L} \mathbf{W}_i^{(c)}[\chi_{i,k|k-1} - \hat{\mathbf{x}}_k^-][\mathbf{y}_{i,k|k-1} - \hat{\mathbf{y}}_k^-]^T \tag{3.21}$$

$$\kappa_k = (\mathbf{P_{x_k y_k}}/\mathbf{S}_{\tilde{\mathbf{y}}k}^T)/\mathbf{S}_{\tilde{\mathbf{y}}k} \tag{3.22}$$

$$\hat{\mathbf{x}}_k = \hat{\mathbf{x}}_k^- + \kappa_k(\mathbf{y}_k - \hat{\mathbf{y}}_k^-) \tag{3.23}$$

$$\mathbf{U} = \kappa_k \mathbf{S}_{\tilde{\mathbf{y}}k} \tag{3.24}$$

$$\mathbf{S}_k = \text{cholupdate}\{\mathbf{S}_K^-, \mathbf{U}, -\mathbf{1}\} \tag{3.25}$$

Where $\mathbf{R^v}$ is process noise covariance, and $\mathbf{R^n}$ is measurement noise covariance. *chol* is a function to computer the Cholesky factorization of a matrix and *qr* is QR Decomposition, for details see [46].

3.4 Experiments

In Raven-II, the tensions can be altered by screw adjusters for each axis. However currently, it is not possible to measure the tension of the cables precisely. Thus, the High and Low tensions were roughly approximated by trial and error measurements on an off-robot pulley-board system by following the steps below:

1. Picked a segment of cable on Raven-II for each joint and measured the length of the segment.

2. Created the same cable segment on the pulley-board.

3. Hanged a known weight on the pulley-board and pushed the middle of the cable segment with a force gauge and measured the force required to give a certain displacement.

4. Repeated step 3 several times with different known weights (displacement is unchanged).

5. Mapped weight applied and force required to push the cable.

6. Gave the same displacement to the cable segments on Raven-II, measured the force required to push the cable to the same displacement, and used the mapping from step 5 to approximate the High and Low tensions.

The steps above were repeated for link 1-3. Table 3.2 shows the approximate tension values for each link.

Joint	High (Kg.)	Low (Kg.)
1	5.2	2.8
2	4.4	1.8
3	4.2	1.4

Table 3.2: Measured cable tensions of each joint.

In the first set of experiments, cable coupling parameter estimation was performed offline to estimate cable coupling parameters for High and Low tensions using the same trajectory. The estimated parameters were used online for state estimation. Next, the following three experiments were performed to investigate the UKF state estimation performance and robustness.

3.4.1 High Tension Performance

- The cable tension of each link was set to the High value.

- The accuracy of joint position estimation during the sinusoidal trajectory was measured and compared with and without the use of the UKF.

3.4.2 Low Tension Performance

- The steps in experiment A were repeated under Low tension.

Experiments A and B allow evaluation of how well the UKF estimates joint position under variations in cable tension. Another parameter which can be easily altered is link mass. In Experiment C, we study the robustness to changes in mass.

3.4.3 Robustness to Added Mass

- The cable tension was set to the High value.
- Robot picked up a 100 g object and the steps in experiments A were repeated.

In these experiments a Proportional Derivative (PD) controller on Raven-II was used to make each link approximately follow a desired sinusoidal trajectory with frequencies 0.3424 Hz for Joint 1, 0.3852 Hz for Joint 2, and 0.4565 Hz for Joint 3. These frequencies were chosen from recorded trajectories of subjects performing the Fundamentals of Laparoscopic Surgery (FLS) [47] block transfer task (to extract frequency components from the trajectory signal, we used FFT and threshold the frequency based on RMS magnitude of the FFT of trajectory). The feedback input of the PD controller was only the motor position.

The input of the system dynamics that is used in the UKF was the generated torque from the PD controller and only motor positions were used as the observation for the UKF online state estimation. In the UKF, α defines the spread of the sigma points around the mean and is set to a small value (1e-3), κ is a secondary scaling parameter and is usually set to 0, and β is used to incorporate the prior use of a distribution. For Gaussian distribution optimal β value is 2 [42]. In this paper the process noise covariance R_v and the measurement covariance R_n are used to control the convergence of the UKF and they do not represent the real noise in the system. For further detail see [34],[35].

3.5 Results and Discussion

Cable coupling parameter estimation for High and Low tensions were estimated offline. The results are shown in Fig. 3.2. Data collected in Experiment A (High tension) is plotted in Fig.

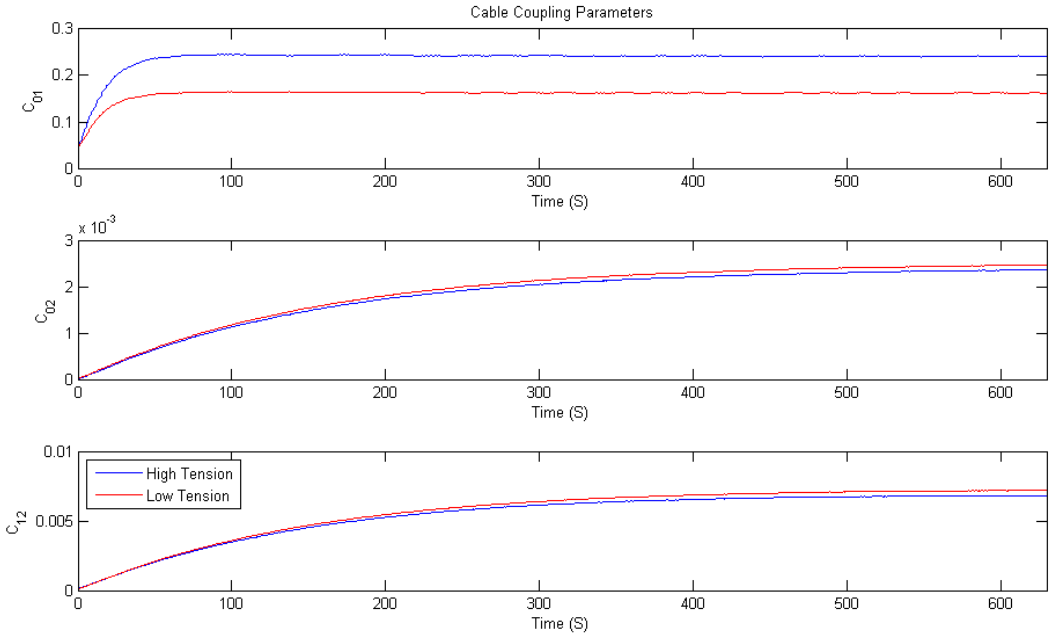

Figure 3.2: Offline Cable Coupling parameter estimation for High and Low tensions.

3.3 which shows the estimated angular position with and without the use of the UKF. The reference true value from the attached optical encoders were also plotted to demonstrate the true joint values. Fig. 3.4 shows the same results collected in Experiment B (Low tension).

Data were also recorded from Experiment C (Fig. 3.5) for position of Joint 1 through 3.

The Mean Absolute Error (MAE) for joint position of all the joints under both tension conditions were calculated with and without the use of the UKF as:

$$\text{MAE} = (1/n)\sum_{i=1}^{n} |(x_{est} - x_{true})| \tag{3.26}$$

The MAE and peak errors for joints 1-3 are shown in Table 3.3.

The percent improvement of the UKF position estimation relative to motor measurements can be computed by Eqn.(3.27). The average MAE position errors and percent improvement

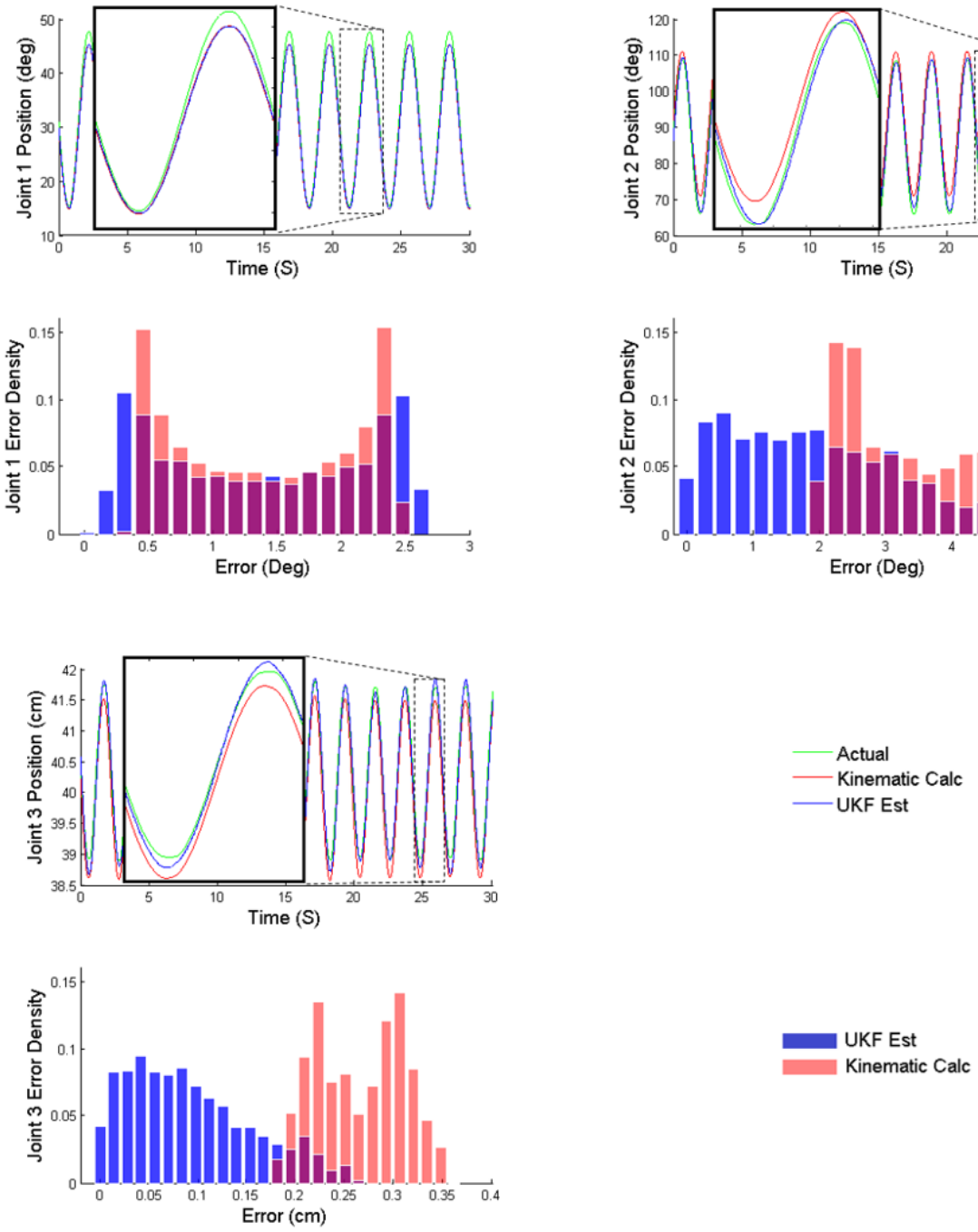

Figure 3.3: Actual, kinematic estimation, and UKF estimation comparison in experiment A. First row shows joint trajectories for joints 1, 2 and 3 respectively; second row shows corresponding error histogram for joint 1, 2 and 3 respectively.

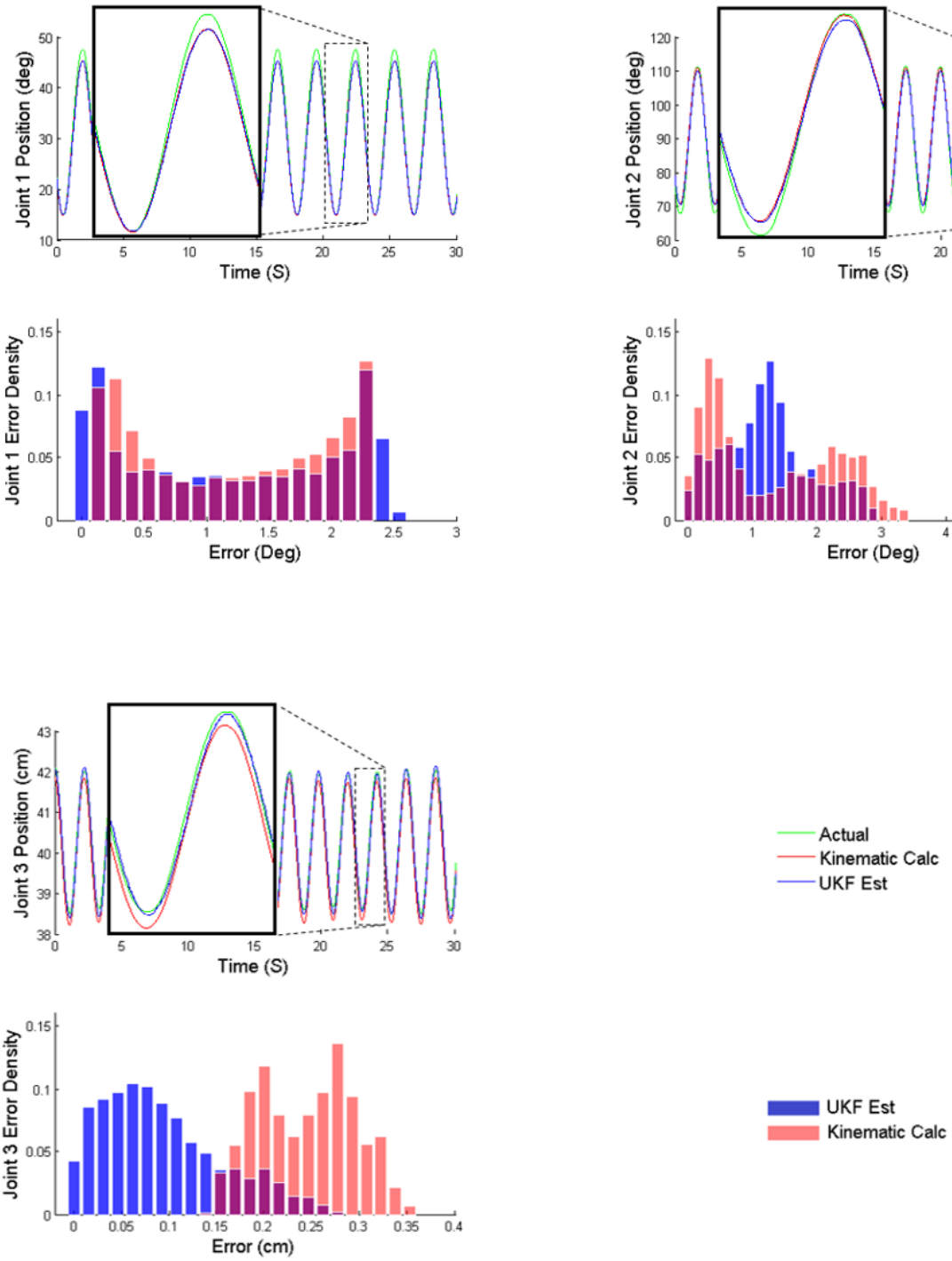

Figure 3.4: Actual, kinematic estimation, and UKF estimation comparison in experiment B. First row shows joint trajectories for joints 1, 2 and 3 respectively; second row shows corresponding error histogram for joint 1, 2 and 3 respectively.

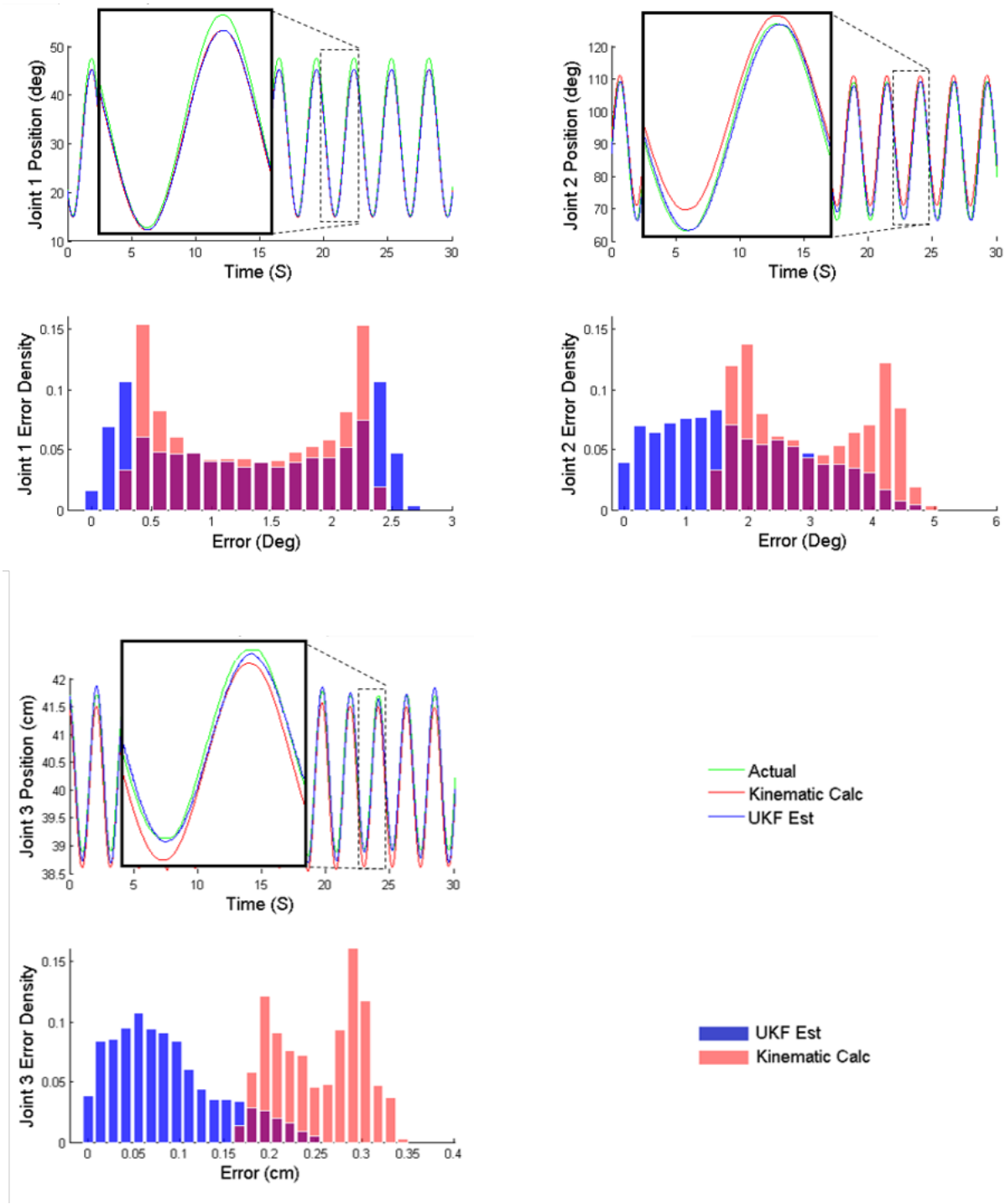

Figure 3.5: Actual, kinematic estimation and UKF estimation comparison in experiment C. First row shows joint trajectories for joints 1, 2 and 3 respectively; second row shows corresponding error histogram for joint 1, 2 and 3 respectively.

Table 3.3: MAE and peak position estimation errors for experiments A-C. Results with greater than 15% difference are shown in bold.

Exp.	Joint	MAE Error		Peak Error		Unit
		UKF	Non UKF	UKF	Non UKF	
A	1	1.3830	1.4070	2.5619	2.4281	Deg.
	2	**1.9394**	3.6137	5.3315	5.6128	Deg.
	3	**0.0929**	0.2647	**0.2634**	0.3538	cm
B	1	1.1945	1.2070	2.5367	2.2899	Deg.
	2	1.2417	1.3023	3.0223	3.3524	Deg.
	3	**0.0927**	0.2437	**0.2907**	0.3593	cm
C	1	1.3063	1.3263	2.6769	2.3506	Deg.
	2	**1.8245**	2.9990	4.6896	4.8877	Deg.
	3	**0.0927**	0.2437	**0.2608**	0.3422	cm

of the three experiments for joints 1-3 are shown in Table 3.4.

$$\%\text{Imp.} = 100 \times (\text{NonUKF}_{\text{est}} - \text{UKF}_{\text{est}})/\text{NonUKF}_{\text{est}} \tag{3.27}$$

Table 3.4: Average position errors and improvement of all the experiments

Joint (Unit)	Avg. UKF MAE	Avg. Non UKF MAE	% Improvement
1 (Deg)	1.2946	1.3134	1.434
2 (Deg)	1.6685	2.6383	36.76
3 (cm)	0.0928	0.2507	62.99

To visualize the error and uncertainty, error bars for all the joint positions experiments A-C are shown in Fig.3.6.

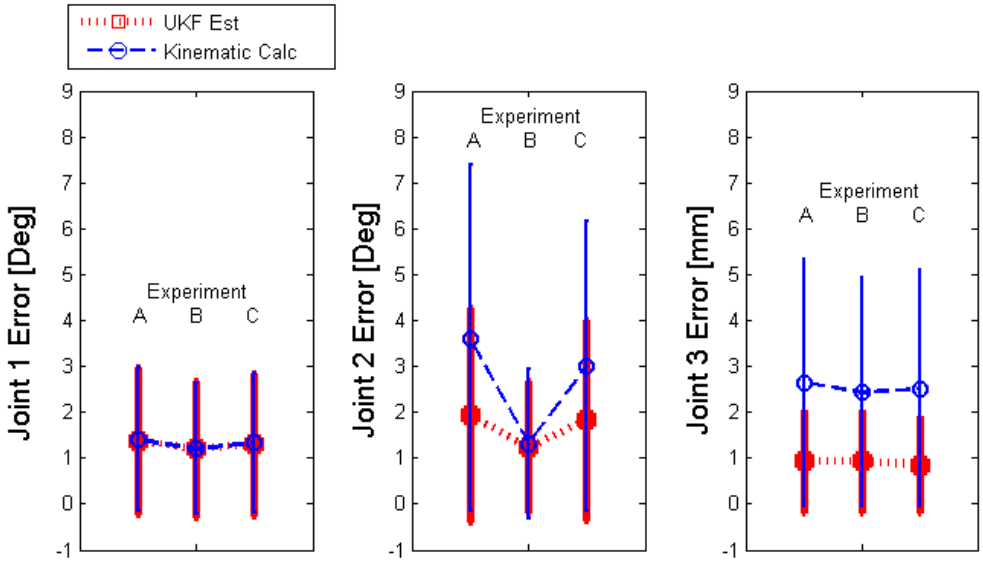

Figure 3.6: Error statistics for position estimation of joint 1-3 for all the experiments; High Tension, A; Low Tension, B; Robustness to Added Mass, C.

The UKF performance was evaluated on Raven but we believe that this work can be extended to any cable driven mechanism. The cable coupling parameters were estimated utilizing the UKF dual parameter and state estimation offline. The observation vector for offline parameter estimation contained both the motor angles and the joint angles. In the experiments online, the UKF outputs and Raven kinematics output without the use of the UKF were compared with installed joint sensors output. The joint sensor outputs were considered as the true value because they are mounted directly on each joint axis.

From Fig. 3.2 all the three cable coupling parameters under both High and Low tensions converged in from 60-500 iterations. The C_{01} which is the cable coupling terms of link 0 to 1 converges in about 60 seconds of robot operation whereas C_{02} and C_{12}, the cable coupling terms of link 0 to 2 and link 1 to 2, converged at a much slower speed to a very small value.

Table 3.3 shows the joint position estimation performance of the UKF for all the three joints. The table shows that the UKF joint position estimation performed better and had better MAE values for all three joints in all cases. Also, the UKF peak error for Joint 2 and 3 was better in all the cases. The joint position estimation of the UKF for Joint 1 was very close to the Raven kinematics output because the length of the cable for Joint 1 is only 5.6 cm, which makes the transmission very stiff, therefore the cable deformation for Joint 1 is negligible. Clearly the UKF will not provide more information if the transmission from motor to joint is highly stiff. When the dynamics of the system is perturbed by changing the cable tension or end-effector inertia, the errors in the UKF estimation are still small compared to the errors without the UKF.

From the error bars in Fig. 3.6, the UKF position estimation is more stable and consistent for joint 2 and 3, which indicates better robustness. In a surgical robot, not only precision but also robustness is important. The robustness is more pronounced in Joint 3, which further indicates that as the link transmission elasticity increases the simple forward kinematic method is not sufficient to estimate states and more sophisticated state estimation method is beneficial. Also, from Table 4.2 it can be seen the percent improvement increases as elasticity increases.

3.6 Conclusion

This Chapter applied the Unscented Kalman Filter to estimate the states of a serial cable driven mechanism using only motor angles on an experimental surgical robot platform (Raven-II) and also investigated the possibility of estimating cable coupling parameters with the UKF. Through the experimental results, it was verified that the UKF position estimation outperforms motor measurements plus kinematics on both precision and robustness. Also, as the transmission stiffness decreases, the use of the UKF is more necessary. Furthermore, the robustness experiments suggest that the UKF is robust to meaningful loads that can be added to the tip of the robot.

Chapter 4

UNSCENTED KALMAN FILTER AND 3D VISION TO IMPROVE CABLE DRIVEN SURGICAL ROBOT JOINT ANGLE ESTIMATION

4.1 Background and Literature Review

In Robotic Surgical Assistants (RSAs), due to sterilization, placement of tracking sensors or encoders on the end-effector is difficult [18]. In Raven, all the encoders are mounted on the shaft of the motors, away from the joints. The joint angles are estimated from **transmission kinematics**: gear ratios, pulley ratios, and cable couplings which define the mapping from motor rotations to joint rotations. Thus, due to elasticity of cables and nonlinear properties [18] the accuracy of cable driven robots are limited. In tele-operating RSAs, these inaccuracies are compensated by the surgeon's visual feedback and skill. However, for autonomous surgical tasks, appropriate control compensation is required.

Stereo vision is becoming more common in RSAs [21]. In [48], 3D visual observations were used to track surgical tools and in [21], stereo vision and a model predictive controller (MPC) were used to correct for these postition errors and perform a simulated debridement task [49, 50] (an automated surgical sub-task to remove dead tissues). In [51], Gaussian Process Regression (GPR)[52], which can be used to learn dynamic models [53], was used to learn accurate kinematic control by including velocity as a feature and removing corrupted observations from a pre-recorded data set. Four high speed cameras with active LED's were used for motion detection and the authors acknowledged the sensitivity of this method to

[1]

sensor noise.

To improve the accuracy of cable driven robots, state estimation techniques can be adopted. Previously the UKF was used in [38] to estimate states of a one DOF cable driven test panel, and in [37], the UKF was applied on a multi-link simulated robot. In Chapter 3, the work on the UKF was extended by applying it to the first 3 DOF of the Raven to estimate cable coupling parameters offline and estimate joint angles online. The UKF improved the state estimation online even by observing only motor encoders. However, in offline parameter estimation, both motor encoders and joint encoders were used to estimate parameters and the feasibility of estimating the system parameters offline without using ideal high resolution joint encoders were not studied. The result showed that for more rigid joints the transmission kinematic errors are dominant and the UKF does not provide improvements. Also, the results were based on an ideal sinusoidal trajectory and statistical analysis were not performed.

In this Chapter, we propose a method to improve the accuracy of position control in RSA with practical sensors. We use added joint sensors only for validation and all the parameter identification is performed with stereo vision and motor encoders. Moreover, we extend the work in the Chapter 3 to 1) estimate kinematic model parameters of the rigid joints in addition to the dynamic model parameters to improve joint angle estimation, 2) perform realistic trajectories to test the effectiveness of the method, 3) verify the system performance and the estimator convergence when the camera is occluded. To evaluate the proposed method, we use the first three DOF of the Raven. The experimental setup is shown in Fig. 4.1.

4.2 Vision

4.2.1 Hardware

We placed a passive visual marker on the tip of the robot and used stereo vision to track the tip in real-time. For stereo vision, we constructed a low cost stereo camera using a pair of "Logiteck QuickCam Communicate MP" cameras with baseline of 48.0 mm and resolution

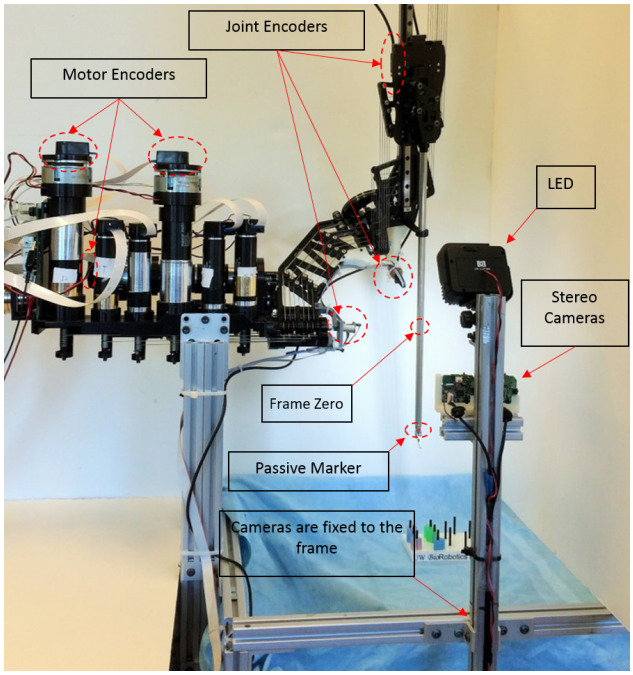

Figure 4.1: Raven-II experimental research platform. Joint encoders are mounted on each joint for validation only and their values were not used in the controller or the UKF. Stereo cameras, fixed perpendicular to the robot base, were used for stereo 3D vision.

of 640x480 pixels at 15 Frame Per Second (FPS). We fixed the cameras perpendicular to the stand of the robot (Fig. 4.1). To calibrate the cameras' intrinsic parameters, we used a checkerboard and the ROS *camera_calibration* package [45]. Once the cameras' intrinsic parameters were known, the translation offset between the origin of the camera frame and the origin of the marker frame (${}^{C}P_{C,M}$) were calculated from the projection of a rectified pixel with disparity to a 3D point.

To register the camera to the robot frame, the transformation between camera frame and the robot frame must be found. In Raven, the location of the end-effector is computed in frame zero [54] and since the cameras are fixed perpendicular to the robot's base, the rotation matrix from cameras to the robot frame zero (${}^{C}_{0}R$) is known. However the translation offset needs to be found.

In Raven, encoders are initialized at the hard-stop position (the physical joint limit position of each joint). Thus at the hard-stop position, there is no kinematic error from cables or coupling matrix. Furthermore, at this position from kinematics, the translation offset between the origin of frame zero and the origin of the end-effector (marker) ${}^0P_{0,M}$ is known. Since in this work, we are only tracking translation, we can assume there is no rotation between frame zero and the origin of the marker (${}^0_M R = Identity$). Thus, the homogeneous transformation from the camera to the marker ${}^C_M T$ is known at this point with translation vector ${}^C P_{C,M}$ and rotation matrix ${}^C_M R = {}^C_0 R$. Also, the homogeneous transformation between frame zero to marker (${}^0_M T$) is known with translation vector ${}^0P_{0,M}$ and rotation matrix ${}^0_M R$. Hence, the transformation from camera frame to frame zero can be calculated by:

$$ {}^C_0 T = {}^C_M T ({}^0_M T)^{-1} \tag{4.1} $$

This method works under the assumption that the camera is mounted perpendicular to the robot and the rotation matrix (${}^C_0 R$) is known. If these constraints are not set, the full transformation can be obtained by placing multiple markers on the tip with known initial kinematics offset at the hard-stop position. However, this still assumes that the camera is fixed to the base.

4.2.2 Methods

To track the end-effector position, we placed a passive color-marker on the tip of the robot and used stereo vision hardware described in Section 4.2.1 for color-marker detection.

Marker Detection

To localize and segment the color-marker, we assumed that no other object with the same color is present in the cameras' field of view. With this constraint, we segment the image with the following procedures. First, we threshold the image based on Hue, Saturation, and Value (HSV). Then, to remove the noise, we smooth the image by applying a median blur filter with kernel size of 5x5 aperture. We also applied the morphological erosion and

dilation operations to remove any potential small blobs. Finally, by applying a contour (chain of vectors around the detected marker) and computing its centroid, we found the pixel location of the origin of the marker for each camera. We use the OpenCV library functions [55] to perform these tasks. To calculate the position of the tip in 3D space, we use ROS *image_geometry* package [45] to find the disparity map between left and right cameras. These procedures are illustrated in Fig. 4.2.

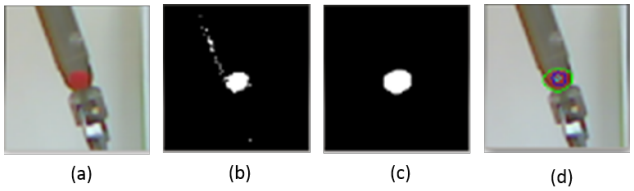

Figure 4.2: Marker detection on square ROI. (a) Original 100x100 ROI image taken from right camera around the tip of the Raven. (b) Thresholded image, (c) Processed image after median filter and morphological operations (d) Fitted circle around the detected segment shown in green.

Performing these tasks for 640x480 pixels is computationally expensive. Also, because the detection is based on HSV, it requires ideal lighting conditions across the workspace. Slight variation in lighting condition may cause no detection at all or multiple false detection. To improve the detection computation performance and reliability we defined a Region of Interest (ROI) based the on current position of the robot.

Region of Interest (ROI)

The kinematics of a cable driven robot may present substantial uncertainties due to lower transmission stiffness. However, the kinematics does provide approximate location of the end-effector from which a ROI can be defined around the tip of the robot. Once a ROI has been implemented, the procedures in Section 4.2.2 can be used to detect and localize the marker. By defining a ROI, the detection computation can significantly be improved. The major advantage of this technique is that the search window of the image is much smaller; therefore,

the lighting condition does not need to be uniform across the entire workspace. Thus, the upper and lower bound of the HSV can be more relaxed. Therefore, slight variations in lighting conditions will not result in multiple false blob detection. Moreover, since with this technique the detection computation is about 31x faster for 100x100 ROI, a pair of high speed cameras' that supports hardware ROI can be used in real-time for high speed robots.

From Raven forward kinematics, we calculate the approximate position of the end-effector and transform this position into the camera frame (${}^{C}P = {}^{C}_{0}T^{0}P$). Then, from the cameras' intrinsic parameters, we project ${}^{C}P$ to pixel space of left and right cameras. The ROI is a square of 100x100 pixels around this position for both left and right image. Once the left and right image is updated with ROI, we use the process outlined in Section 4.2.2 to detect the Raven tip in camera frame and transformed it to robots' frame by ${}^{0}P = {}^{0}_{C}T^{C}P$. Then, inverse kinematics were used to calculate joint angles. Throughout this paper, we denote joint angles based on vision as $\hat{q}_C$.

4.3 Methods

4.3.1 State Estimation

Raven has four states for each link. The states are motor angle, motor velocity, joint angle and joint velocity. However, an optical encoder with 4000 counts per revolution is mounted directly on the shaft of each motor. Therefore, the position and velocity of the motor is well known and equations 2.3-2.5 need not be solved. Using the known motor position of input to the cables of Fig. 2.1, the dynamics can be simplified and the system states can be reduced to two states for each link (joint angle, and joint velocity). With this simplification the state space form of the Raven can be expressed as:

$$\begin{aligned} \dot{\mathbf{x}} &= \mathbf{f}(\mathbf{x}, \mathbf{u}) \\ \mathbf{y} &= \mathbf{H}\mathbf{x} \end{aligned} \tag{4.2}$$

Where $\mathbf{x}$ and $\mathbf{H}$ are system states and the observation matrix, respectively. The system states and observations for the first three links are defined as:

$$\begin{aligned}
\mathbf{x}_i &:= \begin{bmatrix} q_{l_i} & \dot{q}_{l_i} \end{bmatrix}, i = 1, .., 3 \\
\mathbf{x} &= \begin{bmatrix} x_1 & x_2 & x_3 \end{bmatrix}^T \\
\mathbf{h_i} &:= \begin{bmatrix} 1 & 0 \end{bmatrix}, \mathbf{H} = blkdiag(\begin{bmatrix} \mathbf{h_1}, & \mathbf{h_2}, & \mathbf{h_3} \end{bmatrix})
\end{aligned} \tag{4.3}$$

Where i is the link number and the measurements $\mathbf{y}$ are the joint angles based on noisy camera data. In this work, we use the square root (srUKF) [40] form of the UKF which has improved numerical properties [41]. To solve the differential equation, we use the fourth order Explicit Runga Kutta method. The initial inertia matrices, center of mass, and mass were obtained from CAD models and the joint friction parameters (F_{cl}, F_{vl}) were obtained from Chapter 2.

4.3.2 Parameter Estimation

Raven system consists of both kinematic model and dynamic model parameters. We used the dual srUKF method from Chapter 3.2.2 to estimate these parameters and equation (4.3) is used for state space representation of states.

Kinematic Model Parameters

Many cable driven mechanisms, have gear ratios, cable pulley ratios, and mechanism kinematics. It is very important to know the exact value of each of these parameters for accurate transmission kinematics calculations. Slight variation in any of these parameters can substantially increase the error in calculating the end-effector position from motor angles alone. In Raven, the transmission of joint 1 is very stiff. Thus, transmission kinematic error is dominant vs. error due to cable compliance. This, was observed in Chapter 3, where the UKF did not provide any improvements for estimating the joint angles of rigid transmissions.

From kinematics of Raven, the motor angle of link 1 is related to joint 1 angle by: $q_m = N(r_{l1}/r_{m1})q_1$. Where, $N = 12.25$ (gear ratio), $r_{l1} = 63.095mm$ is the design radius of the partial pulley of link 1, and $r_{m1} = 5.675mm$ is the design radius of the motor capstan.

However, as it can be seen from Fig. 4.3 (b) there is a gap between the pulleys which introduces uncertainty in the pulley ratio. This causes significant error in joint angle estimation. In Raven software, we modeled the r_{l1} with different radii and we used physical measurements to observe the change when r_{l1} radii value is change by -10% to +10%. We used the joint encoder for our physical measurements. Fig. 4.3 (a) shows when r_l is change by -5%, the error decreases to almost zero. To compensate for this source of error, we used the dual UKF parameter estimation and stereo vision to estimate the radius of partial pulley of link 1 (r_l).

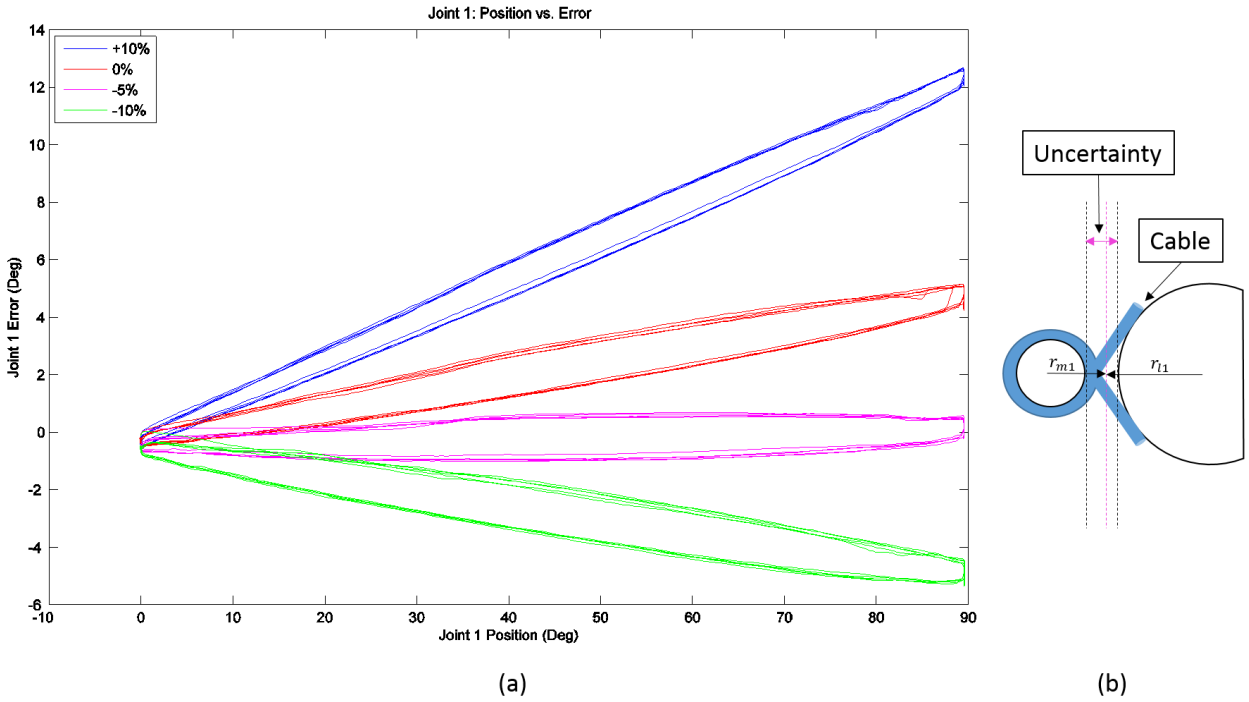

Figure 4.3: (a) Computed Joint 1 position error when the value of r_{l1} is changed by +10%, 0%, -5%, -10%. The error decreases to almost zero when the value is changed from its design value by -5%. (b) Schematic drawing of link 1 transmission shows uncertainty in transmission ratios.

Dynamic Model Parameters

Over time, the cable parameters such as stiffness and damping can change due to creep and stretch [18, 38]. We used the dual UKF parameter estimation and stereo vision offline to compensate for these changes to improve system dynamics.

4.4 Experiments

In this Chapter, the main objective is to improve the state estimation of the joint angles by using the srUKF and low cost stereo vision. Therefore, to measure the performance of the srUKF, additional optical encoders were installed on the joints for comparison. Fig. 4.4 shows a block diagram representation of the joint angle computations and measurements. q represents the true joint angle. $\hat{q}_{Kin}$ is the estimated joint angle based on transmission kinematics. $\hat{q}_C$ is the estimated joint angle based on camera raw data, and $\hat{q}_{UKF}$ is the estimated joint angle based on UKF method proposed in this Chapter. With Raven we conducted Fundementals of Laparoscopic (FLS) block transfer task [47] and we recorded all the Raven states for Joints 1-3. Block transfer task is one of the five FLS tasks that emulates tissue handling and manipulation [56]. In this task, the user grasps the object with their non-dominant hand, transfers the object mid-air to the dominant hand, and places the object on a peg.

To estimate parameters and states of the Raven, we used our pre-recorded FLS task trajectory for experiments B-D.

4.4.1 Kinematic Model Parameters Estimation

To improve the state estimation, we first estimated the partial pulley radius (r_l) of link 1 offline using the UKF parameter estimation. To estimate r_l of link 1, we ran a sinusoidal trajectory on Raven and we observed the end-effector with the cameras. These observations were used in the UKF dual parameter and state estimation offline.

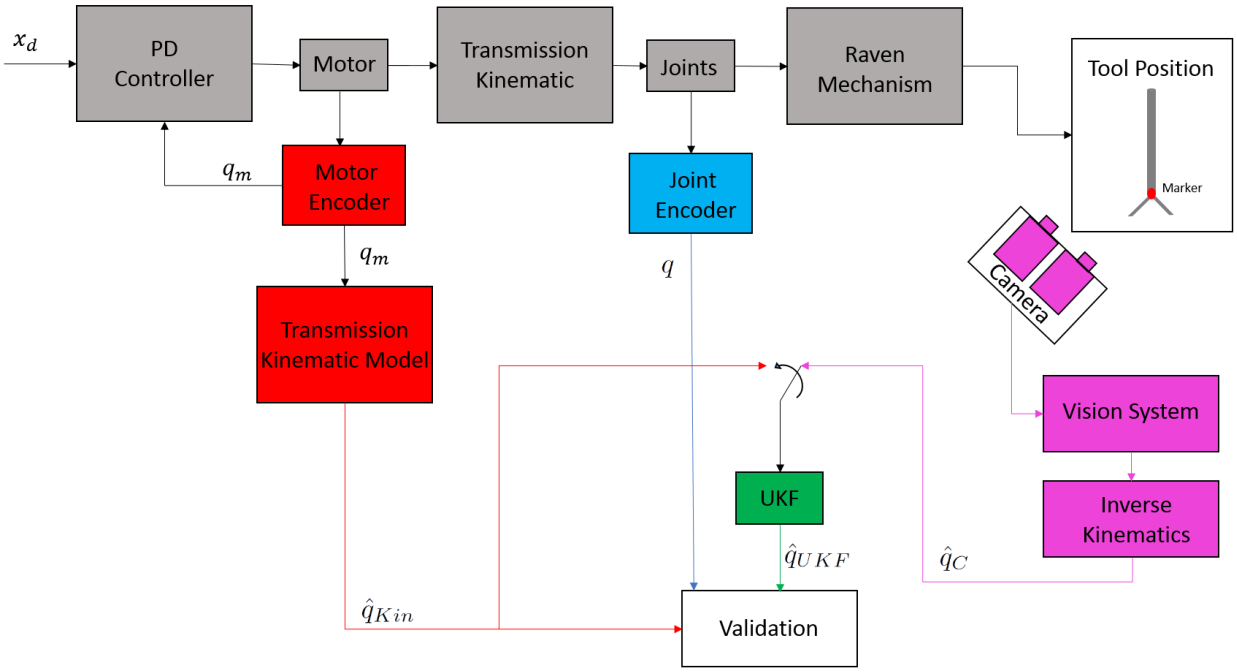

Figure 4.4: Block diagram of the controller loop and joint angles. x_d is the desired trajectory. q is the true joint angle measurements from optical encoders mounted directly on the joints. $\hat{q}_{Kin}$, $\hat{q}_C$, and $\hat{q}_{UKF}$ are estimated joint angles from transmission kinematics, camera, and UKF, respectively. The robot controller feedback is based on the motor measurements and not the UKF. When occlusion happens the UKF observation will switch from $\hat{q}_C$ to $\hat{q}_{Kin}$.

4.4.2 Dynamic Model Parameters Estimation

After finding the updated value of r_l for link 1, we estimated the cable parameters. To estimate cable parameters, a pre-recorded FLS block transfer trajectory was performed by Raven and the cable stiffness (k_e) and cable damping (b_e) parameters of joints 1-3 were estimated with the dual UKF.

4.4.3 State Estimation

After finding the kinematic and dynamic model parameters offline, we used the updated parameters to estimate system states online. To test state estimation under realistic conditions, FLS block transfer trajectories in free-space were applied to the control inputs of the Raven PD controller. To conduct statistical analysis, we ran the robot six times with different pre-recorded FLS block transfer trajectories. Each experiment had a different duration. The total length of all these six experiments were 900 seconds.

4.4.4 Camera Occlusion

The UKF is programmed to detect occlusion. UKF detects occlusion when no marker is detected in either of the cameras or if the marker jumps to a new location. To investigate the system performance and filter convergence under camera occlusion, five experiments with the same FLS block transfer trajectory of 200 seconds were conducted. Each experiment had occlusion for a different percentage of time: 10%, 20% , 40%, 60%, and 80%. To simulate occlusion, we repeatedly blocked the camera data for multiple intervals of 2 seconds at equal time intervals to create the above percentages. During the camera occlusions, the UKF joint observations were changed to $\hat{q}_{Kin}$ with a hard switch (Fig. 4.4). $\hat{q}_{Kin}$ is calculated from transmission kinematics based on motor encoder measurement.

4.5 Results and Discussion

4.5.1 Experiment A

The radius of the partial pulley of the link 1 (r_l), was estimated based on a 200 seconds sinusoidal trajectory (Fig. 4.5). The parameter estimation (Fig. 4.6) converged in about 40 seconds to 59 mm from the initial value of 63.095 mm or a decrease of 6.49%. This is a consistent with experimental results of Fig. 4.3. From Fig. 4.3, it can be seen that a decrease of about 5% is required in the value of the pulley ratios to minimize the kinematic error.

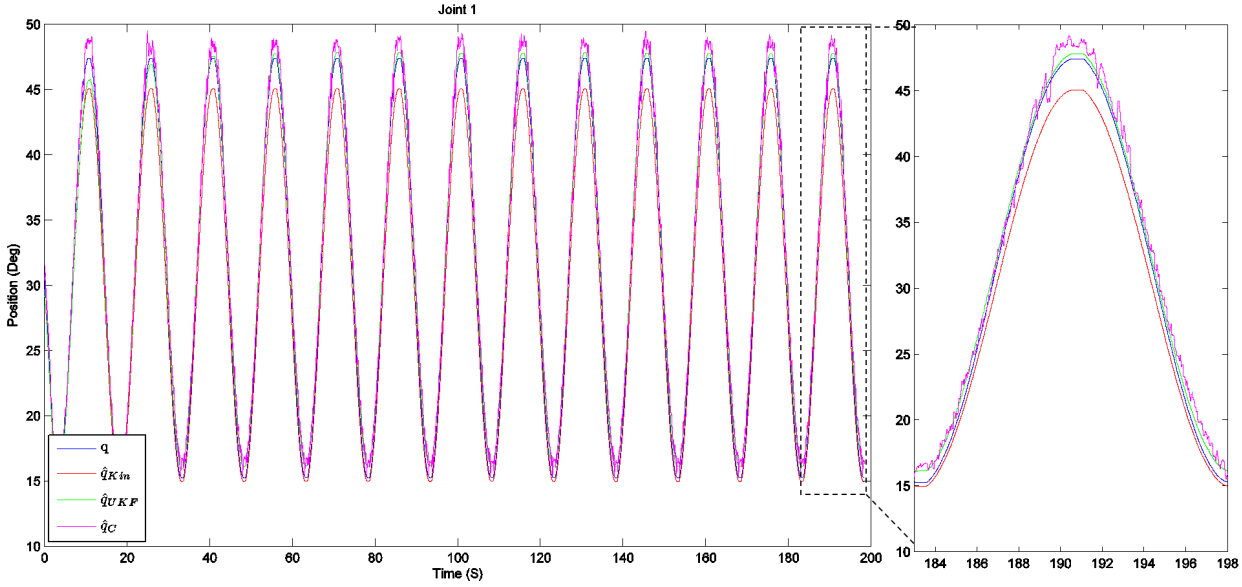

Figure 4.5: Plot showing the true position (q, blue), transmission kinematic estimate ($\hat{q}_{Kin}$, red), UKF estimate ($\hat{q}_{UKF}$, green), and camera estimate ($\hat{q}_C$, magenta). This sinusoidal trajectory was performed by Raven to estimate r_l.

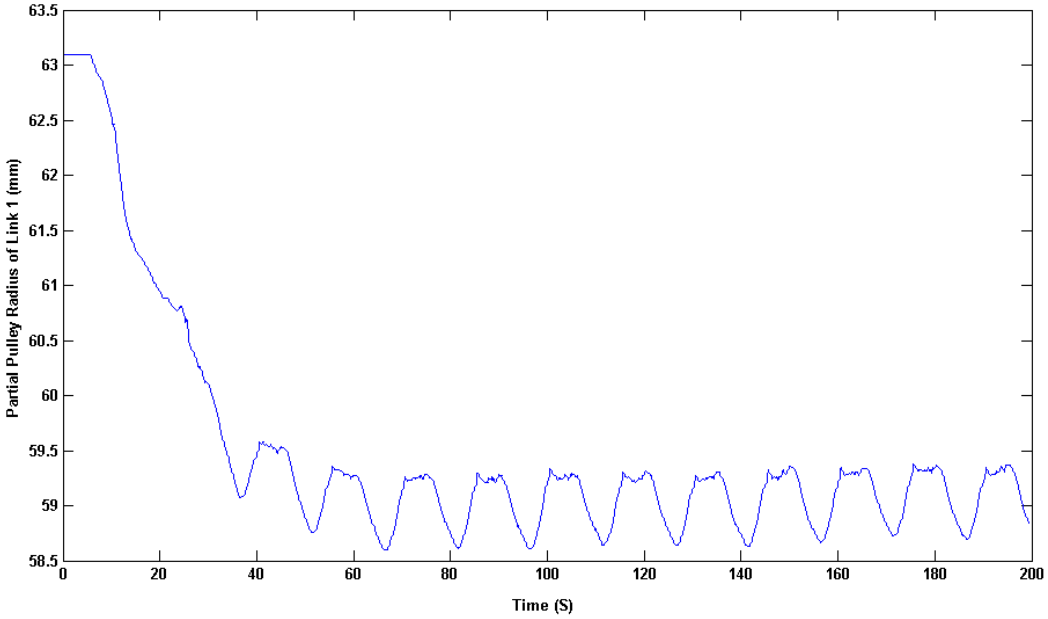

Figure 4.6: Estimated r_l parameter for link 1.

4.5.2 Experiment B

The dynamic model parameters of the cables, i.e. stiffness and damping, were estimated based on 200 seconds of a pre-recorded FLS trajectory. The results are shown in Fig. 4.7. The damping values of link 1 and 2 converged in about 100 seconds and the stiffness values of joint 1 and 2 converged in about 150 seconds. The stiffness value for joint 3 stayed at about the same value and the damping value converged at about 80 seconds.

4.5.3 Experiment C

The updated parameters were used for state estimation. Six different FLS block transfer trajectories were performed by the robot. The first FLS trajectory is shown in Fig. 4.8. The figure illustrates the estimated joint angles with the UKF and direct transmission kinematics for joints 1-3. The joint angles based on camera data and the reference true value from attached joint encoders were also plotted. The corresponding error histogram is shown in

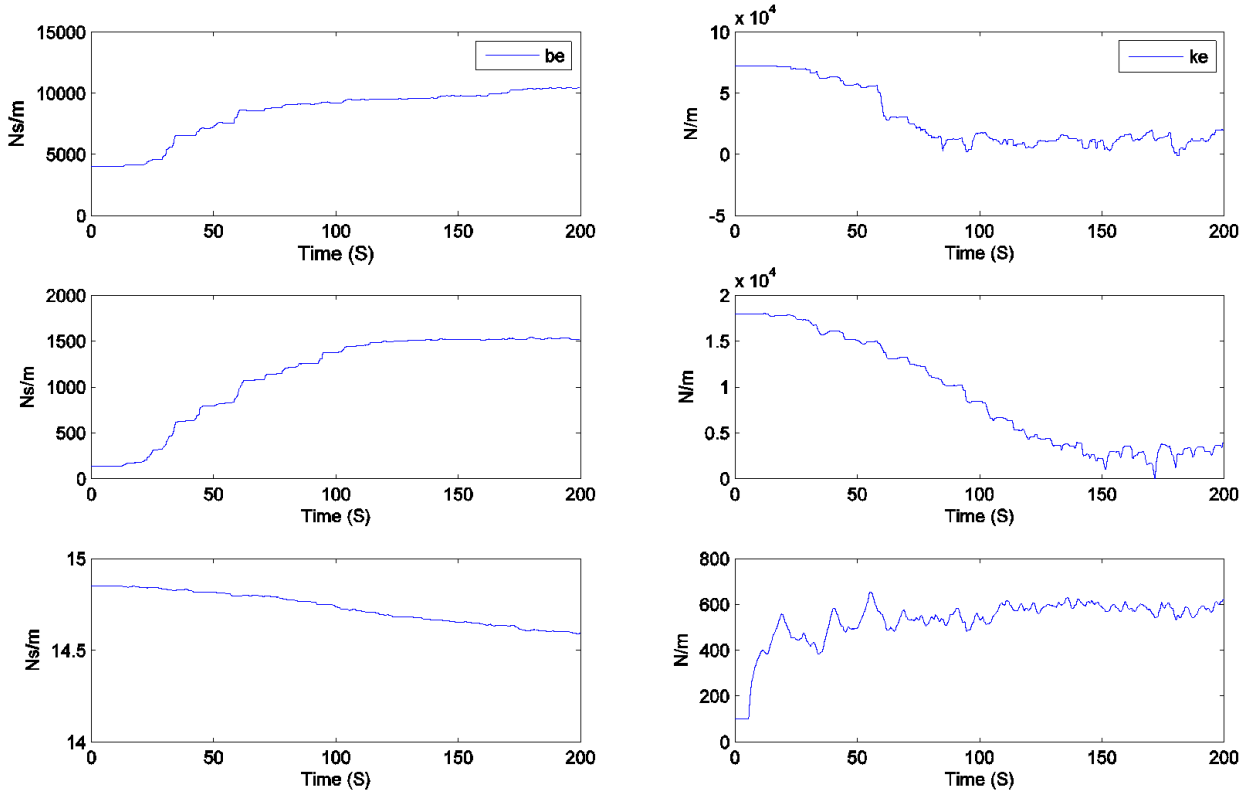

Figure 4.7: Estimated cable parameters (stiffness and damping) for link 1-3 from top row to bottom row, respectively.

Fig. 4.9. The error using the UKF joint angle estimation for all three joints is less than the error using the direct transmission kinematics method. The results for joints 2 and 3 are comparable with Chapter 3 where joint encoders were used to tune system parameters. Moreover, the result for the rigid joint is substantially improved due to kinematic model parameter estimation.

The results for the remaining five experiments were similar and in all the cases the UKF outperforms transmission kinematics. To perform statistical analysis and summarize the results of all these six experiments the box plot of all these experiments are shown in Fig. 4.10-4.12 for joints 1-3, respectively. Furthermore, the joint angle Mean Absolute Error (MAE) using UKF ($e_{\hat{q}_{UKF}}$) and the joint angles MAE using transmission kinematics ($e_{\hat{q}_{Kin}}$)

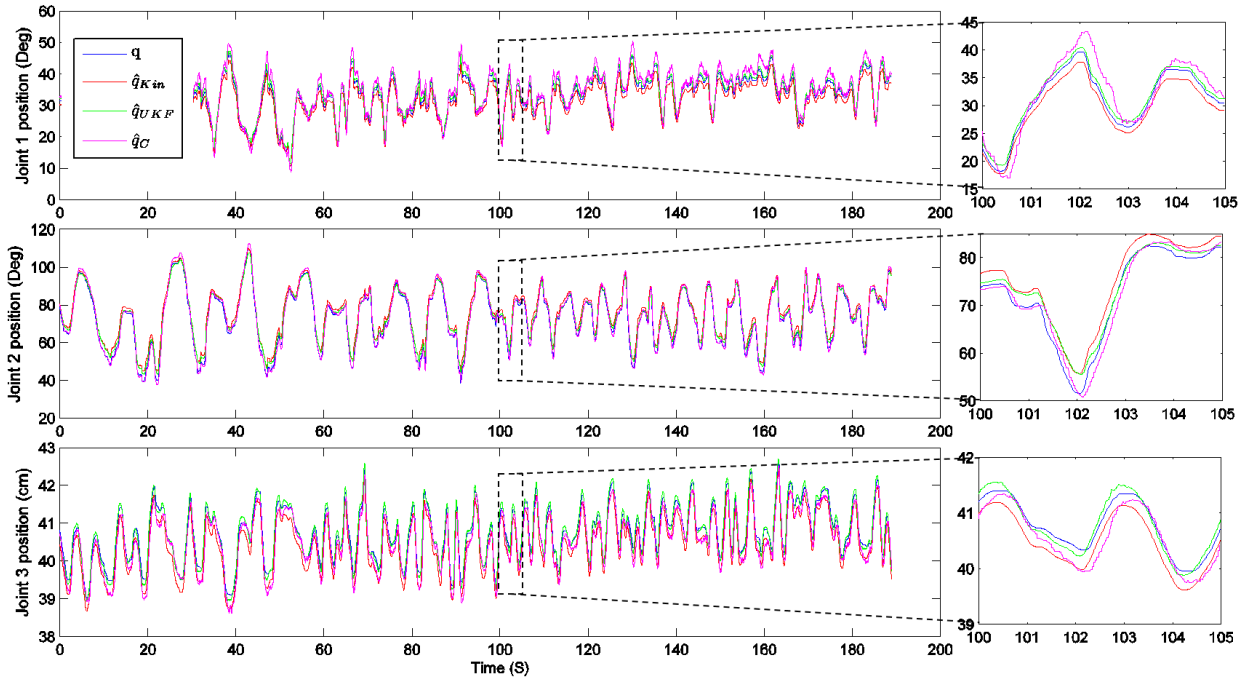

Figure 4.8: Actual, transmission kinematics, camera, and UKF estimation of trial 1. Rows 1-3 shows joints 1-3 trajectory, respectively.

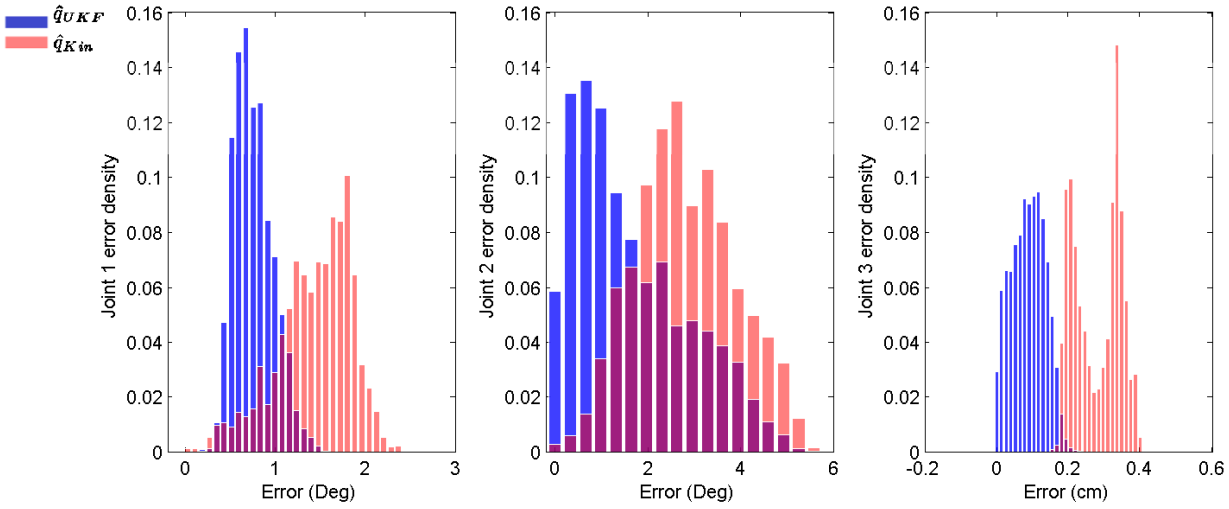

Figure 4.9: Error histogram of trial 1 trajectory for joints 1-3 from left to right, respectively.

for joints 1-3 of trials 1-6 are shown in Table 4.1 for comparison. From the table $e_{\hat{q}_{UKF}}$ is less than $e_{\hat{q}_{Kin}}$ for all three joints in all the trials. We took the average of all the trials and use $(100 \times (e_{\hat{q}_{Kin}} - e_{\hat{q}_{UKF}})/e_{\hat{q}_{Kin}})$ to find the percentage improvement that the UKF provides over direct transmission kinematic method for joint angle state estimation. The mean and percent improvements are shown in Table 4.2. When the average was weighted by experiment duration, the results were the same. Also, to verify if there are statistical difference between the $e_{\hat{q}_{Kin}}$ and $e_{\hat{q}_{UKF}}$ we applied Student's t-test. The P values for the t-test are shown in table 4.2. From the t-test it can be concluded that there are significant difference between two groups.

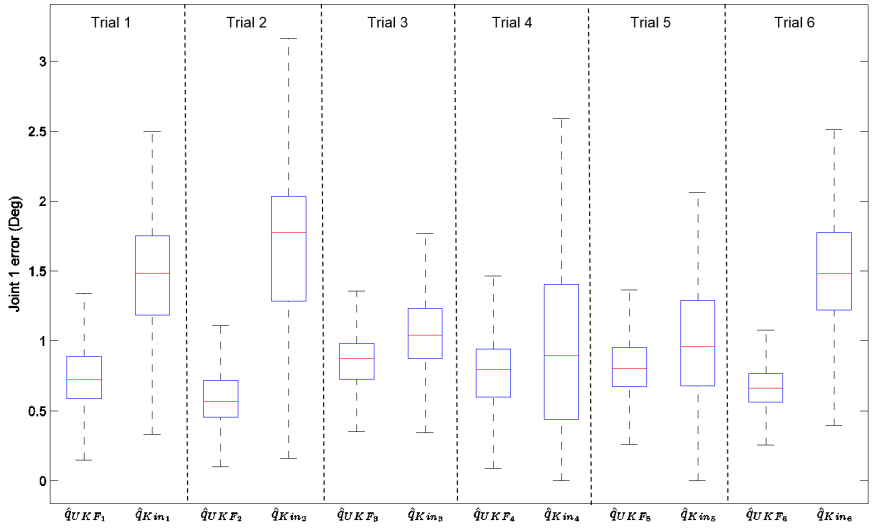

Figure 4.10: Boxplot showing the results for Experiment C, for trials 1-6 for joint 1. For each trial, boxplot of UKF estimate and direct transmission estimate is shown for comparison. The UKF estimate error is less than direct transmission estimate for all the six trials.

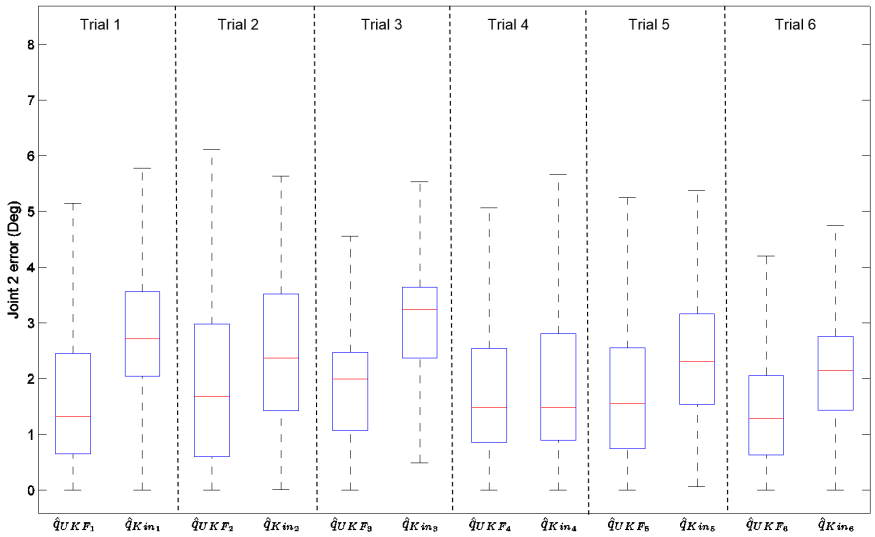

Figure 4.11: Boxplot showing the results for Experiment C, for trials 1-6 for joint 2. For each trial, boxplot of UKF estimate and direct transmission estimate is shown for comparison. The UKF estimate error is less than direct transmission estimate for all the six trials.

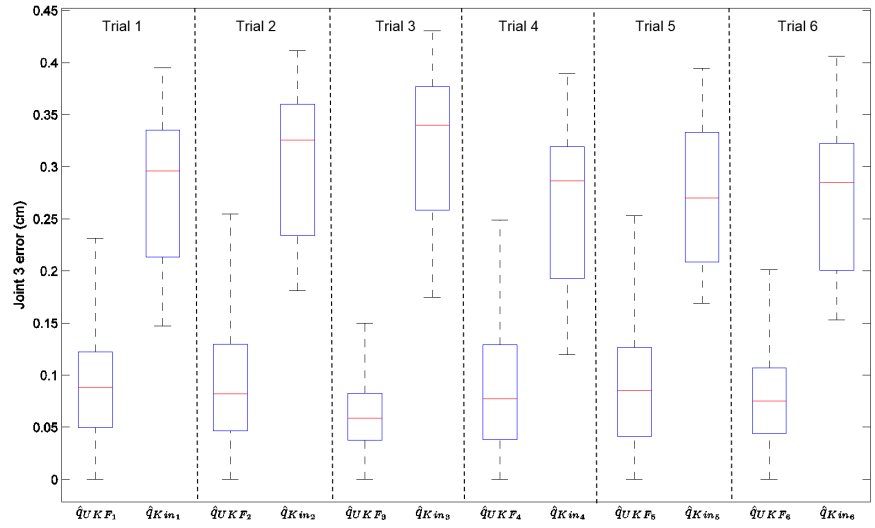

Figure 4.12: Boxplot showing the results for Experiment C, for trials 1-6 for joint 3. For each trial, boxplot of UKF estimate and direct transmission estimate is shown for comparison. The UKF estimate error is less than direct transmission estimate for all the six trials.

Table 4.1: MAE position estimation errors of joints 1-3 for Experiment C trials 1-6.

		Joint 1 (deg)	Joint 2 (deg)	Joint 3 (cm)
Trial 1	$e_{\hat{q}_{UKF}}$	0.7525	1.6373	0.0869
(188 sec)	$e_{\hat{q}_{Kin}}$	1.4294	2.8012	0.2792
Trial 2	$e_{\hat{q}_{UKF}}$	0.5958	1.8665	0.0989
(80 sec)	$e_{\hat{q}_{Kin}}$	1.6644	2.5525	0.3036
Trial 3	$e_{\hat{q}_{UKF}}$	0.8414	1.7965	0.0606
(150 sec)	$e_{\hat{q}_{Kin}}$	1.0847	2.9971	0.3227
Trial 4	$e_{\hat{q}_{UKF}}$	0.7881	1.7541	0.0852
(82 sec)	$e_{\hat{q}_{Kin}}$	0.9313	1.9428	0.2647
Trial 5	$e_{\hat{q}_{UKF}}$	0.8167	1.7644	0.0852
(110 sec)	$e_{\hat{q}_{Kin}}$	0.9827	2.3691	0.2730
Trial 6	$e_{\hat{q}_{UKF}}$	0.6825	1.4220	0.0763
(290 sec)	$e_{\hat{q}_{Kin}}$	1.4675	2.1314	0.2675

Table 4.2: Average position errors and percent improvement of trials 1-6 for joint 1-3.

Joint (Unit)	$e_{\hat{q}_{UKF}}$	$e_{\hat{q}_{Kin}}$	% Improvement	P value
1 (Deg)	0.7419	1.3051	43.14	0.0025
2 (Deg)	1.6411	2.4652	33.42	0.0015
3 (cm)	0.0790	0.2828	72.05	2.59e-9

4.5.4 Occlusion

The results for occlusion experiments are shown in Fig. 4.13 (a-c) for links 1-3, respectively. We expected that as the occlusion percentage increases, the joint angle estimation error would also increase. However, only slight degradation in quality of state estimation was observed for joint 2 and 3. On the contrary, the estimation for joint 1, improved slightly as the occlusion percentage increased. We believe this is because the camera is perpendicular to link 1. Thus, joint 1 is based on the cameras depth measurement (the cameras depth measurements are much more noisier than x and y measurements). Overall, only slight degradation and improvement was observed for joint 1-3 as the percent occlusion increased; and therefore, from this experiment, it can be concluded that the UKF estimation is consistent even when occlusion is likely to occur in an application. This suggests that once the system parameters have been identified and fine tuned offline with the UKF and the camera, the UKF will have sufficient information from motor encoders to consistently estimate the states.

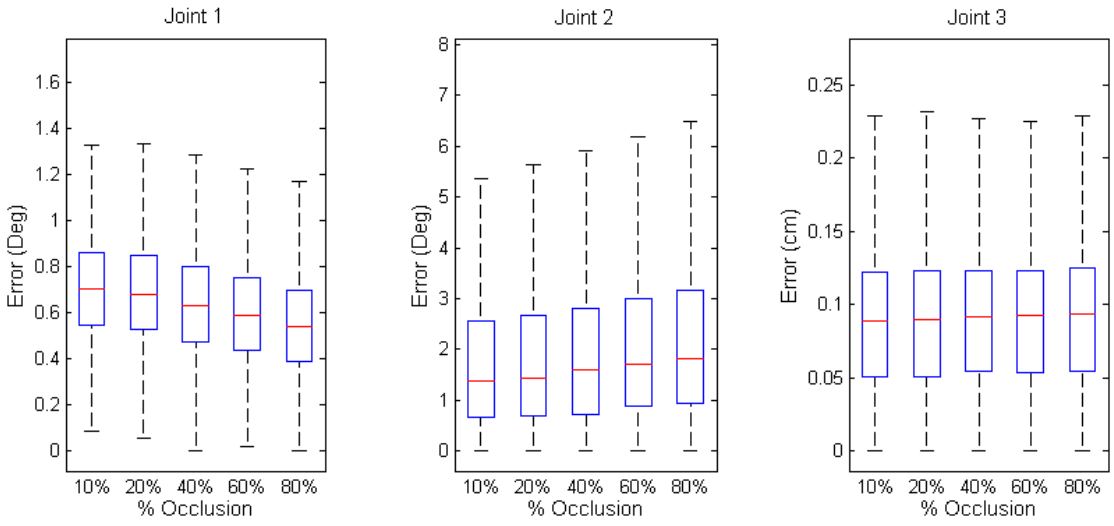

Figure 4.13: Boxplot showing the results for Experiment D, for joints 1-3 from left to right, respectively. Each plot shows a boxplot for 10%, 20%, 40%, 60%, and 80% occlusion. From the boxplot, the occlusion does not degrade the performance of the UKF state estimate.

4.6 Conclusion

In this Chapter, we used motor encoders and low cost cameras to estimate joint transmission parameters of rigid link (joint 1 is considered rigid, because the cable length for link 1 is very short comparing to the other links of Raven), cable parameters for all the links (joints 1-3), and joint states of a serial cable driven robots on the Raven experimental surgical robot platform utilizing the Unscented Kalman Filter. With this method, we were able to fine tune the system dynamics by estimating parameters offline. Once the dynamics were tuned with UKF parameter estimation, the UKF was able to improve the joint angle estimation. The occlusion experiment suggests that this method is reliable and robust even when the camera is occluded during state estimation. From the experiments, once the system parameters are tuned with stereo vision and the UKF offline, the camera measurements did not provide much improvement online during state estimation. Hence, only motor measurements and UKF will be sufficient. This is beneficial because in practice the camera will get occluded during surgery. However, running both the camera and motor encoder at the same time improves safety due to redundancy that is provided to estimate joint angles.

Chapter 5

UTILIZING ELASTICITY OF CABLE DRIVEN SURGICAL ROBOT TO ESTIMATE CABLE TENSION AND EXTERNAL FORCE

5.1 Background and Literature Review

In Robotic Surgical Assistants (RSA) haptic feedback is still severely impaired while being very important for surgeons [10]. Also, in cable driven RSA's cables are pre-tensioned to avoid slacking. The amount of pre-tension affects system dynamics such as friction and cable elasticity [18]. In this Chapter we propose a method to estimate cable pre-tesnsion and also estimate external forces acting on the end-effctor to address haptic feedback.

5.1.1 Cable Tension

In cable driven manipulators, power is transmitted through tension to driven axes. To avoid slacking, the cables must remain under tension [16, 18]; so, cables are pre-tensioned. Too much pre-tension causes faster wear and tear, and reduces the lifetime of the cables. Not enough pre-tension causes slack and degrades the performance of the robot. In [18], it was verified experimentally that if the amount of pre-tension is not considered in the controller, the steady state error of the robot increases. Therefore, to have optimal performance, it is necessary to know the amount of pre-tension. However, cable properties changes overtime due to creep, stretch, and wear of strings of the cable [18, 38], which change the amount of pre-tension over time. Hence, it would be beneficial to have a method that indirectly estimates the cable's pre-tension to improve both the performance of the robot and its

[1]

lifetime. In some surgical robots direct measurements of cable tension may not be possible due to sterilization or cost requirements; thus, tension must be estimated indirectly. In [18], it was found that among system parameters (i.e stiffness, damping, friction, etc.), stiffness has the largest correlation with the amount of pre-tension. The stiffness correlation was studied in experiments in which tension was varied and measured in each step. The method of [38] was used to estimate system parameters for each tension value and a curve was fit. This was verified on a 1-DOF pulley-board that simulates a cable drive system. Being able to estimate cable tension indirectly could 1) avoid requirements of expensive tension sensor, 2) improve the control performance by considering the changes in system dynamics, 3) alert users if the tension is outside of safe operation regions [18]. In this Chapter we extend this work by applying the UKF parameter estimation and stereo vision from Chapter 4 to estimate cable pre-tension on the third link of the Raven-II [13] surgical system.

5.1.2 Haptic Feedback

A study by Wagner et al, showed the performance of the RSAs can be greatly improved with force feedback [57]. Conventionally, surgeons use haptic feedback to palpate tissues as one of their diagnostic tools to figure out if a tissue is normal or not [1]. With haptic perception, surgeons can feel tissue hardness, measure tissue properties, and detect if a tumor is hidden under the tissue [10]. Also, when imaging methods does not view tissue lesions clearly [58], haptic feedback can be used to get information regarding locations and dimensions [59–63]. Moreover, with lack of haptic feedback, surgeons may exert excessive force to a healthy tissue or apply deficient forces in tissue handlings such as grasping and suturing [64]. There are numerous approaches to address the lack of force feedback in RSAs. In [10] Puangmali et al. describes several methods including displacement-based, current-based, pressure-based, resistive-based, capacitive-based, piezoelectric-based, vibration based, and optical-based sensing. In [64] Quasi-Static Modeling of da Vinci instrument which takes distribted friction and tendons compliance into account was proposed and it was used in [65] to estimate the stiffness of the environment by appliying a sufficiently large input torque. In

[66], a special mechanism was made with a spring and a fixed spherical visual feature. With this sensor, as the distance between the camera and feature changes, force can be estimated from the visual appearance of the feature [66]. In [58], a distal sensor for MIS palpation was built. In [67], a computerized force feedback endoscopic surgical grasper (FREG) was developed to recover the tactile and kinesthetic information. In [68], on a pulley board that simulates 1-DOF cable driven robot, system dynamics was used with Unscented Kalman Filter (UKF) to estimate contact force and position in free motion and in contact with tissue. This system dynamics were further extended in [69] and Chapter 2 of this thesis along with cable couplings that exist in a serial cable driven robot to apply the UKF on the first 3DOF of the Raven-II. In [70], the dynamics and UKF from [69] and Chapter 3 of this thesis were further used to estimate grasping force acting on Raven-II graspers by observing motor torques. However, the motors that were used in [68], and [70] were small and have less noise than the bigger motors that are used in the first 3-Dof of the Raven-II. Also, this method only demonstrated external forces acting on one quadrant and the other quadrants were not investigated.

In this Chapter, we use the UKF method and apply it on link 3 of the Raven-II which has a bigger motor with higher variance noise torque plot, and we investigate the results on all the four quadrants. Moreover, we also used elasticity of the cables similar to series elastic actuators to estimate forces on all the four quadrants and we compared this method with the UKF.

The main contributions of this Chapter are:

- Investigated the feasibility of estimating the cable pre-tension based on dynamical model presented in Chapter 2 and 3.

- Estimated external forces acting on the robot in all the four quadrants based on UKF, and cable elasticity.

- Compared in detail external force estimation using both methods.

- Force estimation results, based on sinusoidal trajectories and recorded human operator-driven trajectories from block transfer (FLS) tasks.

To evaluate the effectiveness of the proposed methods, the prismatic joint of the Raven-II (third link) was used to estimate cable tension and external forces.

5.2 Tension Estimation

5.2.1 Method

The goal of this section is to indirectly derive cable pre-tension based on dual srUKF parameter estimation of Chapter 3.2.2. To indirectly estimate cable pre-tension in a cable driven robot, the stiffness parameter of the dynamic modeling of Chapter 2 was used. The observation vector for srUKF to estimate the k_e were camera measurements and motor encoders. To get the tension ground truth value, we used vibration frequency of the cable to indirectly measure tension. The following steps were used to estimate cable pre-tension based on srUKF parameter estimation:

1. Get relationship between frequency to tension from an offline pulley board.

2. Vary tension experimentally using tension screws, measure cables vibration frequency, and use srUKF to estimate k_e.

3. Use tension relationship derived in step 1 to convert frequency value of step 2 to tension. With this we can derive the relationship between tension and k_e.

5.2.2 Experiments and Results

Due to mechanical design of the Raven-II it is not simple to measure the cable tension directly with a force gauge or a tension meter. Therefore, to measure the cable pre-tension ground truth, cable vibration frequency was used instead. Cable has different vibration frequencies at different tensions. To measure the vibration frequency, a frequency reader with piezoelectric

sensor and Arduino was built. To map cable vibration frequency to tension, a known weight was hung on an offline pulley board that resembles link 3 of the Raven-II (same cable length). Then the cable was plucked with a guitar pick to vibrate the cable, and a piezoelectric sensor was used to read its vibration frequency. This experiment was repeated with several different known weights to get enough data to map cable vibration frequency to tension. Fig. 5.1 shows the frequency to tension mapping.

The trend line equation for Fig. 5.1 is:

$$Tension \quad = 0.0009f^2 + 0.0412f - 2.3769 \tag{5.1}$$

where, f is frequency in Hz.

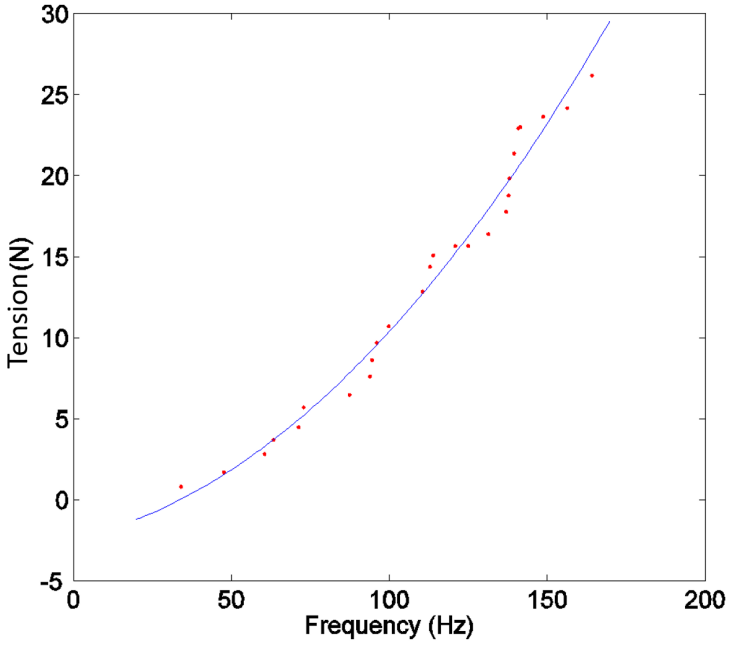

Figure 5.1: Frequency (Hz) to Tension (N) mapping.

Raven-II has a tensioner screw for each link for adjusting the tension. To map the stiffness to tension, the cable tension of the Raven-II was changed for a total of 18 times by adjusting

the tensioner screw and its vibration frequency was measured each time. Then, the measured frequency was converted to tension based on Eqn. (5.1). At each different tension, the robot moved by the same pre-recored Fundamentals of Laparoscopic (FLS) block transfer task trajectory (described in Section 4.4) and the srUKF was used to estimate the cable stiffness for each run. The initial value of the k_e was set to 600 (N/m). Fig. 5.2 shows the convergence of the srUKF stiffness estimation for all the 18 runs.

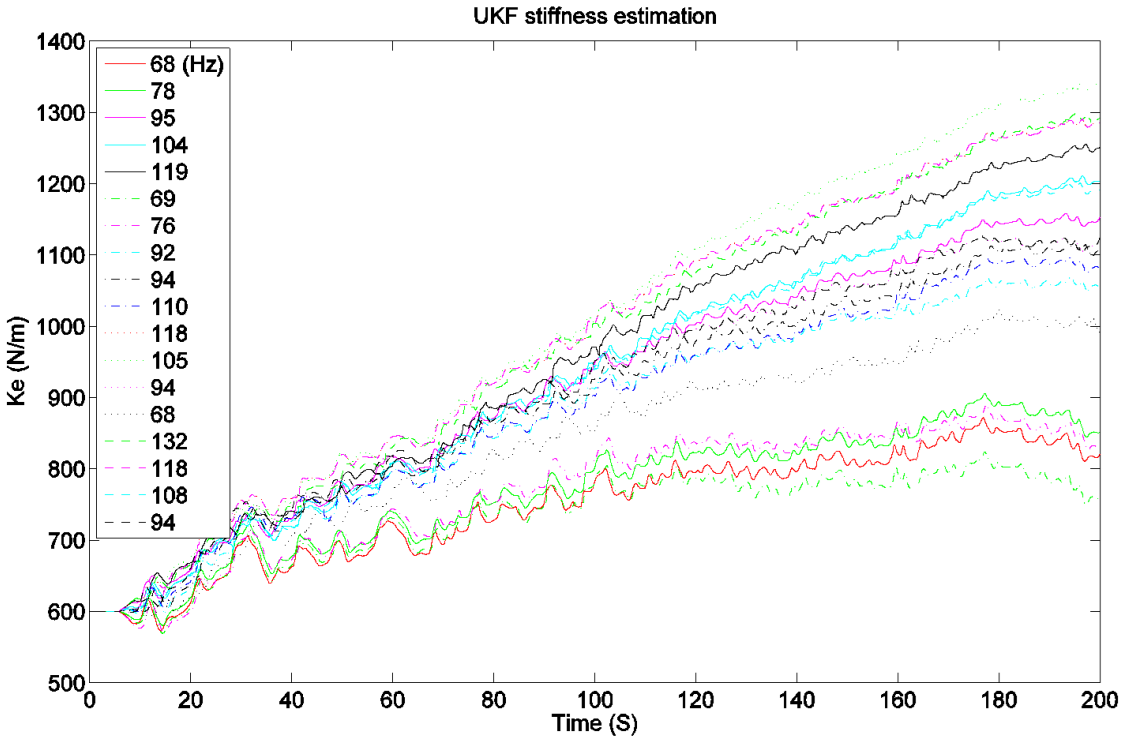

Figure 5.2: UKF stiffness estimation convergence for 18 runs at different vibration frequency (Hz) for each run. For each run, cable tension was manually changed, its vibration frequency was measured and the stiffness value k_e was estimated with srUKF. The robot moved by the same pre-recorded FLS trajectory for all the runs.

To map stiffness k_e to tension indirectly, we used a 100 second window on Fig. 5.2 and averaged the k_e parameter over a period of 100 seconds. Fig. 5.3 (a) shows the mapping from

cable stiffness to tension obtained by fitting a degree-two polynomial between cable stiffness and known tension which was calculated from Eqn. (5.1). From the plot it can be seen that as the stiffness increases the cable pre-tension also increases. Based on this mapping, cable pre-tension estimation can be categorized into three different categorizes (Low, Mid, High), where Low is less than 8N, Mid is between 8-14N and High is above 14N. Thus, by estimating the k_e with srUKF and using the mapping from Fig 5.3 (a) it can be determined in which category tension falls. Ideally, the tension should be in the Mid level, since if the tension falls in the low level there is a chance that cable can become slack. Finally, if the tension falls in the High level the cable lifetime decreases substantially.

The trend line equation for Fig. 5.3 (a) is:

$$Tension \quad = 1.0504e - 4{k_e}^2 - 0.1583k_e + 64.4230 \tag{5.2}$$

where, k_e is the estimated stiffness value. Also, to see the effect of changing the window size, we changed the window size to the last 20 seconds of Fig. 5.2 and averaged the k_e parameter over a period of 20 seconds. Fig 5.3 (b) shows the change when the window size is changed to the last 20 seconds.

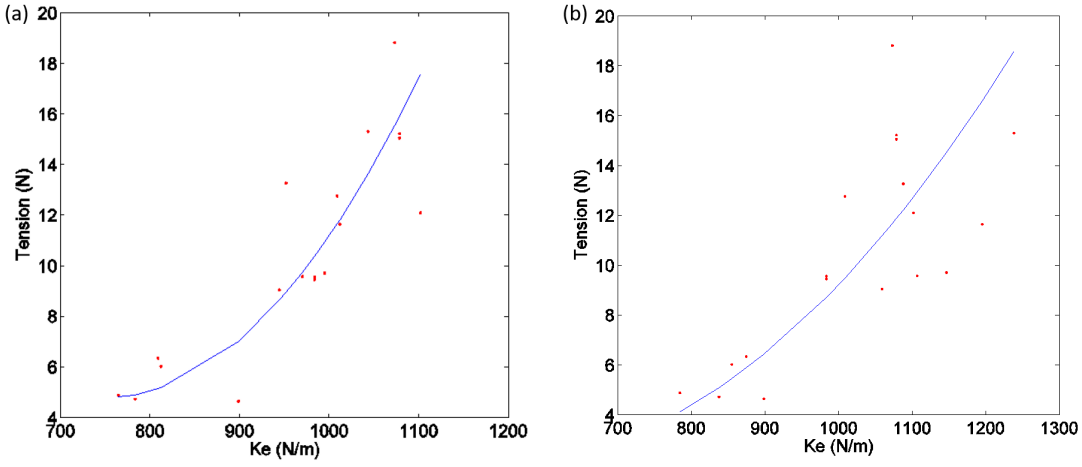

Figure 5.3: Showing a degree-two polynomial that maps cable stiffness to tension (N). (a) with window size of 100 seconds, (b) with window size of last 20 seconds.

5.3 Force Estimation

5.3.1 Methods

External forces acting on the robot can be categorized in four quadrants. We define these four quadrants as follows:

Quadrant I: Motor torque is (+), external force (F_{ex}) is (+)*. In this quadrant the displacement of link 3 is positive (link is moving up) and external force is acting against the displacement (motor requires more torque to move the link).

Quadrant II: Motor torque is (+), F_{ex} is (-). In this quadrant the displacement of link 3 is positive and the external force is helping the motor.

Quadrant III: Motor torque is (-), F_{ex} is (-). In this quadrant the displacement of link 3 is negative (link is moving down) and external force is acting against the displacement.

Quadrant IV: Motor torque is (-), F_{ex} is (+). In this quadrant the displacement of link 3 is negative and external force is helping the motor.

In this Chapter external force acting on a cable driven robot is investigated by two different methods. These methods are verified on the third link of the Raven-II system. The first method is based on dual srUKF state and parameter estimation by observing motor torques only, while the second method is based on the elasticity of cable by measuring the stretch in cable similar to Series Elastic Actuators (SEA) [24]. Fig. 5.4 shows the cable stretch and motor torque plot of link 3 when a basket with four different weights (271g, 497g, 704g, and 910g) is lifted up and down in a sinusoidal motion. From these plots, both motor torque and cable stretch can be used to infer external forces acting on the robot. (Note: these weights are randomly selected to show the significant variation in motor torque and cable stretch. Any weights can be selected to serve the same purpose.) By visual inspection it can be that concluded at 271g it is easier to detect the force from cable stretch than motor torque. This implies the cable stretch method can detect smaller forces better than UKF and motor torque observation. Fig. 5.5 shows the way in which four quadrants

[1]* External Force sensor read positive for contact force in the direction of gravity.

can be categorized from torque and cable stretch measurements.

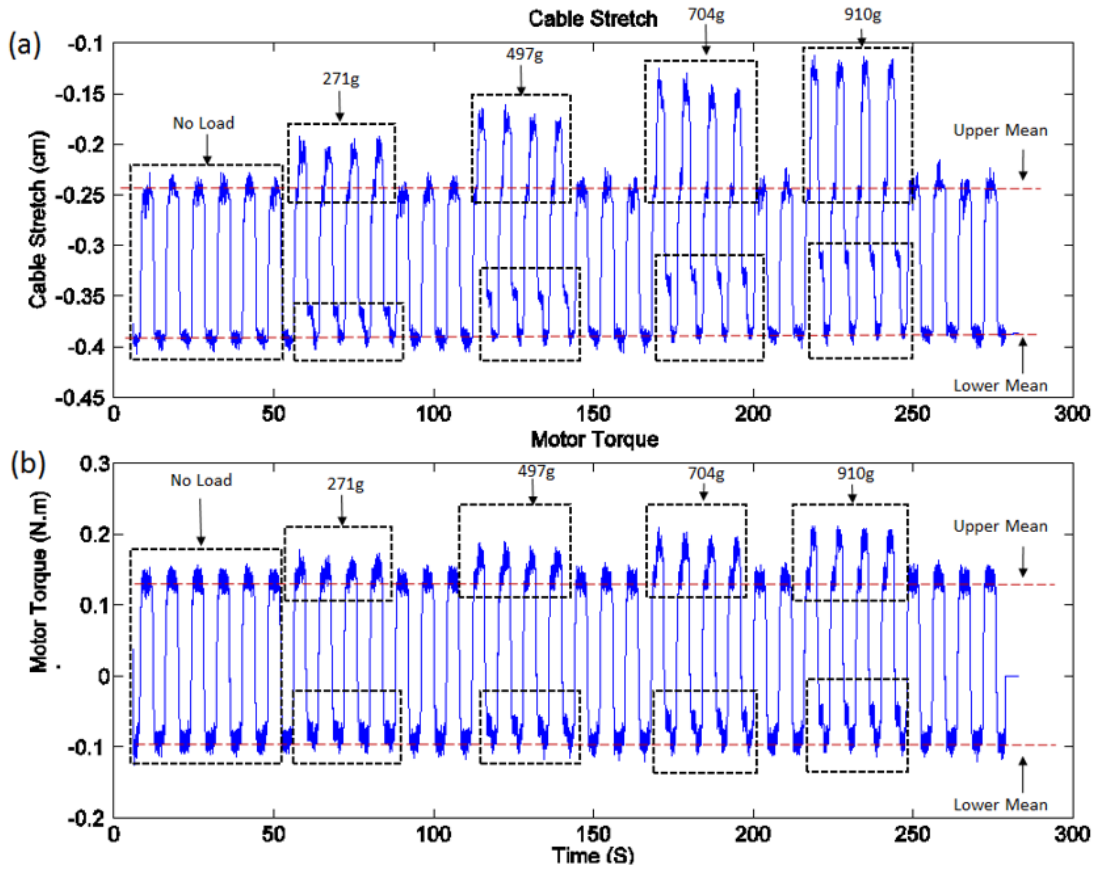

Figure 5.4: (a) Cable stretch and (b) Motor torque when a weight is lifted up and down. No external force is present in the first six cycles. 271 gram weigh is hung on the second four cycles, and then no load is present in the next 2 cycles. This is repeated with 497g, 704g, and 910g respectively.

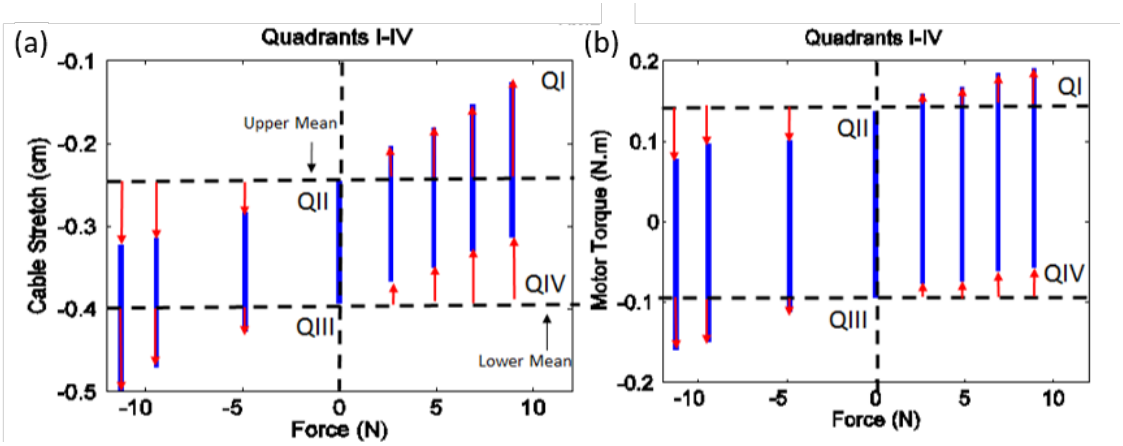

Figure 5.5: four quadrants categorization from (a) cable stretch and (b) torque measurements, Q I and Q IV is from lift experiment and Q II and Q III is from pushing compression spring experiment. Blue bar represents the raw measurements for cable stretch and torque, while red arrow represents the stretch value and torque difference used for force estimation value.

UKF Method

To estimate external forces acting on the third link, first system dynamic parameters F_c and k_e were estimated offline using dual srUKF parameter estimation technique as described in section 5.2.1 by setting the F_{ex} term of Eqn. (2.2) to zero. Once the system parameters were tuned offline, the external forces could be estimated online by srUKF parameter estimation.

Cable Stretch Method

In this method, precise measurement of cable stretch is required. In Raven-II, optical encoders are mounted on the motors away from the joints. However, for this experiment an additional linear optical encoder (MicroE Systems, model number Mercury II 1600, resolution 5 μm) was attached directly to link 3 to directly measure joint displacement θ_J (in Raven Joint 3 is prismatic joint and the displacement is in cm). With the motor encoders, the **transmission kinematics** [71] from Chapter 4 was used to calculate joint angles $\theta_{J_{Kin}}$ based on kinematics. In Eqn. (2.6), the cables were modeled as non-linear exponential tension-strain. However, from Fig. 5.3 (a), (stiffness to tension mapping) it can be seen that at low pre-tension, the curve is highly non-linear and at higher tension, the curve is more linear. For estimating the external force, since there exist pre-tension in cable, it was assumed the force will lie in the linear region. Therefore, we used Hook's law to estimate external force. From Hook's law the external force can be described as:

$$F_{ex} \quad := K_s(\theta_{J_{Kin}} - \theta_J) \tag{5.3}$$

where K_s is the spring constant and $(\theta_{J_{Kin}} - \theta_J)$ is cable stretch. From Fig. 5.4 (a) the cable stretch value is negative and also it's not zero when no external forces are present. This is due the initial offset that presents between the motor and joint encoders because of encoder initialization, cable pre-tension, and friction. To be able to estimate the force based on cable stretch this amount of offset needs to be identified. Fig. 5.6 shows the cable stretch histogram for the first six cycles of the lifting basket experiment. These initial cycles can

be used as the training phase and during this phase two Gaussians can be fit to the data. The mean of each Gaussian with +/- one sigma were used to initialize the cable stretch and determine the upper mean, lower mean, and the mid point. The motor is connected to the joint via two cable runs (Fig. 2.1). Thus, any cable stretch above mid point is caused by one cable and any stretch below the mid point is caused by the other cable which means the stretch sign could change.

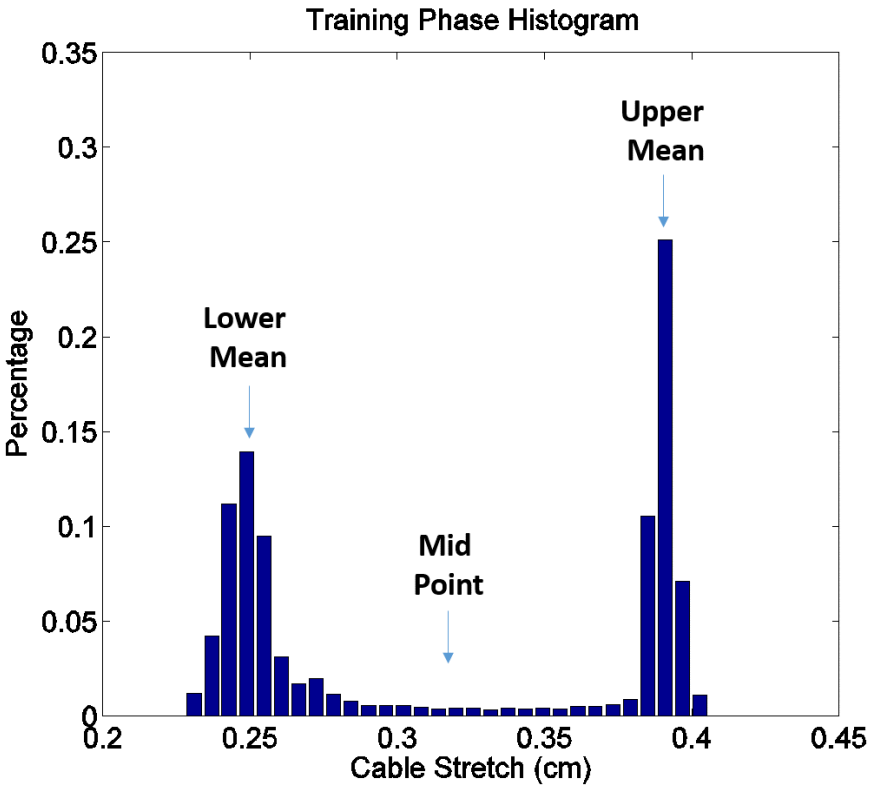

Figure 5.6: Histogram of cable stretch when no load is present in the first six cycles of the lifting basket experiment. From the histogram upper mean, lower mean, and the mid point of the cable stretch can be identified.

Once the cable stretch is initialized, the stretch measurements need to be identified for each quadrant. Fig. 5.7 shows the way in which cable stretch measurements are assigned to

each quadrant. This can also be seen from Fig. 5.5 (a). If cable stretch is more than the upper mean, force belongs to quadrant I; if the stretch measurements are less than the upper mean and more than the mid point, force belongs to quadrant II; if stretch is less than the lower mean, force belongs to quadrant III; and finally if stretch is less than the mid point but more than the lower mean, force belongs to quadrant IV. However, if stretch is +/- one sigma from the midpoint, force is in unknown state. Throughout this work, anytime cable stretch falls into unknown state UKF estimation results were used instead.

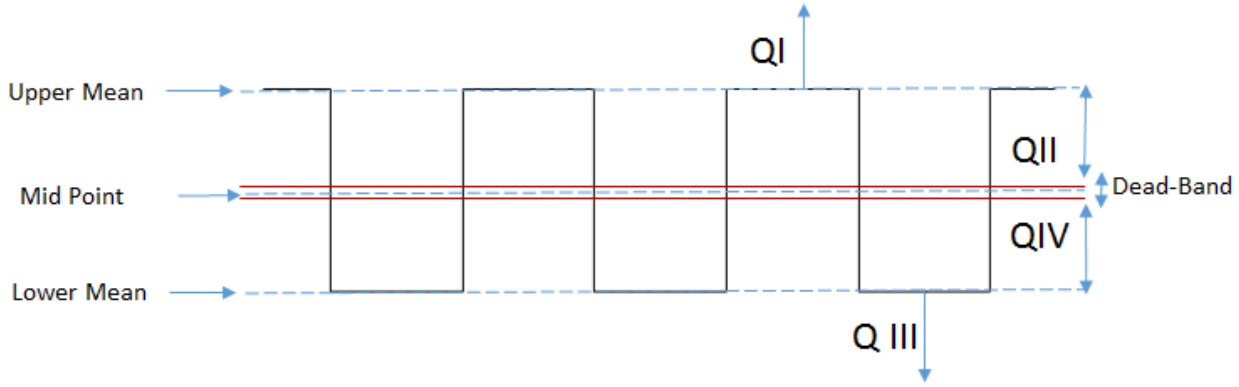

Figure 5.7: Four quadrants categorization based on cable stretch.

5.3.2 Experiments and Results

The proposed methods were applied to the third link of Raven-II cable driven surgical robot which is the linear tool insertion link. In the experiments, the first two links were held still in an angle that makes link 3 perpendicular to the surface and only the linear motion insertion link moves. The following six experiments were conducted to estimate F_{ex} utilizing both the UKF and cable stretch method.

Experiment 1: Zero Force Estimation

The proposed methods were applied when no external forces were present. In this experiment, Joint 3 followed a sinusoidal trajectory in a free motion. Ideally the true F_{ex} value should

be zero since no external force is present. Fig. 5.8 (a) shows the estimated force based on the cable stretch. From the plot it can be seen that there is a peak error every time torque changes direction. In other words, this error occurs at the beginning of force estimation in quadrants II and IV. Closer inspection of the cable stretch plot suggests that at the moment when robot displacement changes direction, there exists a linear delay in cable stretch which suggests damping. This problem can be treated by putting a linear damper in (5.3). Fig. 5.8 (b) shows the zero force estimation based on the series elasticity and a linear damper. By adding a linear damper (5.3) becomes:

$$F_{ex} \quad = K_s S + b\dot{S} \tag{5.4}$$

where S is cable stretch, b is the cable damper term and $\dot{S}$ is stretch rate of change.

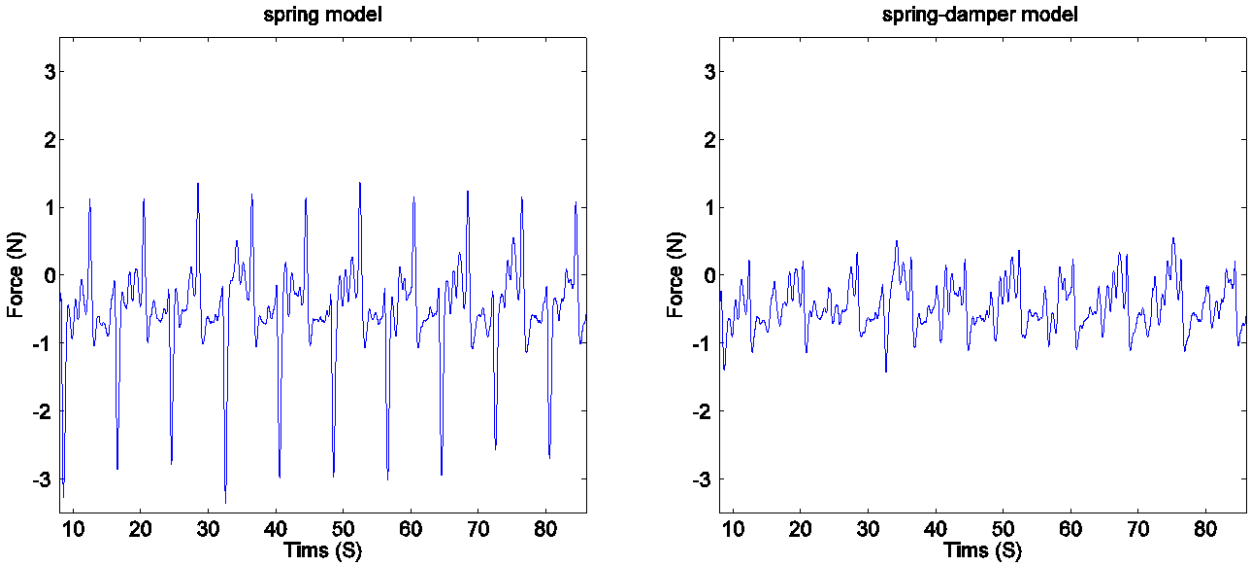

Figure 5.8: Zero force estimation using cable stretch method with (a) linear spring model (b) linear spring and a linear damper model.

Fig. 5.9 shows the error histogram for both UKF and cable stretch methods when the damper term is added to the cable stretch model (5.4). From the error histogram the noise

for UKF method is from -3N to 2.5N while the noise for cable stretch method is from -1.4N to 0.5N.

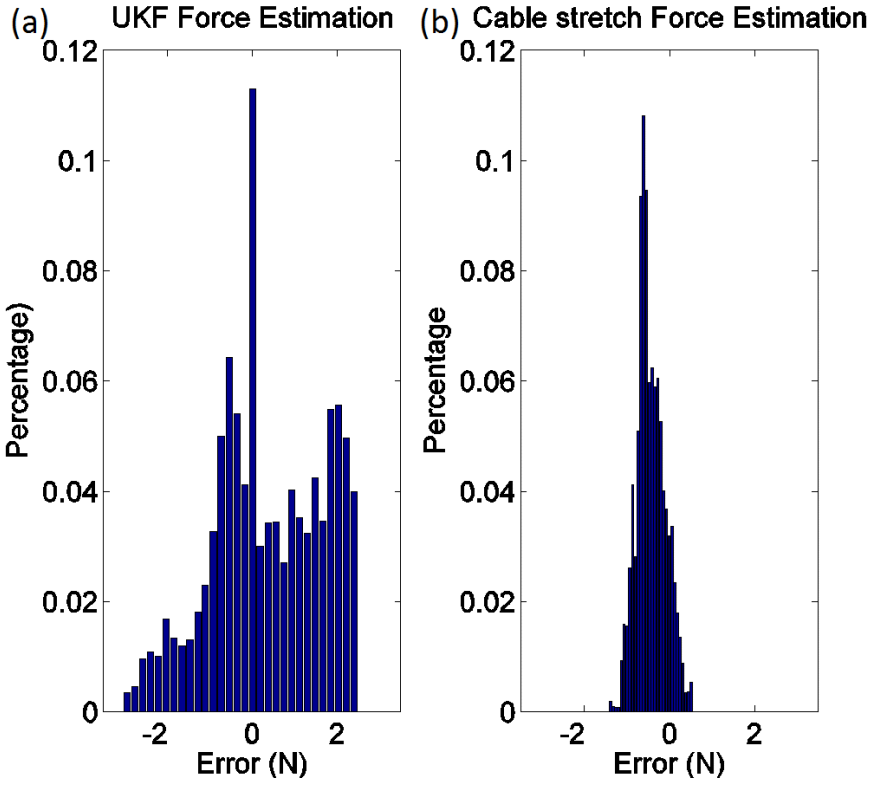

Figure 5.9: Zero force estimation error histogram for (a) UKF and (b) Cable stretch.

Experiment 2: Lifting Basket

In this experiment, a sinusoidal trajectory was applied to the third joint while lifting a basket up and down with known weights. The weights hanging on the basket were 271g, 497g, 704g, and 910g, respectively. This experiment was used to calibrate the force estimation in quadrants I & IV. Peak values from the cable stretch (Fig. 5.4 a) were subtracted from the upper mean and lower mean for quadrant I and IV, respectively for each weight, and a line was fit to estimate the K_s value and the offset. The b value was manually selected to minimize the transition error.

Fig. 5.10 shows the force estimation results for both UKF and cable stretch method. Since this experiment was used to calibrate estimation, it is expected that the estimation result is close to the real values. However, it can be seen with the UKF method the noise variance is much larger.

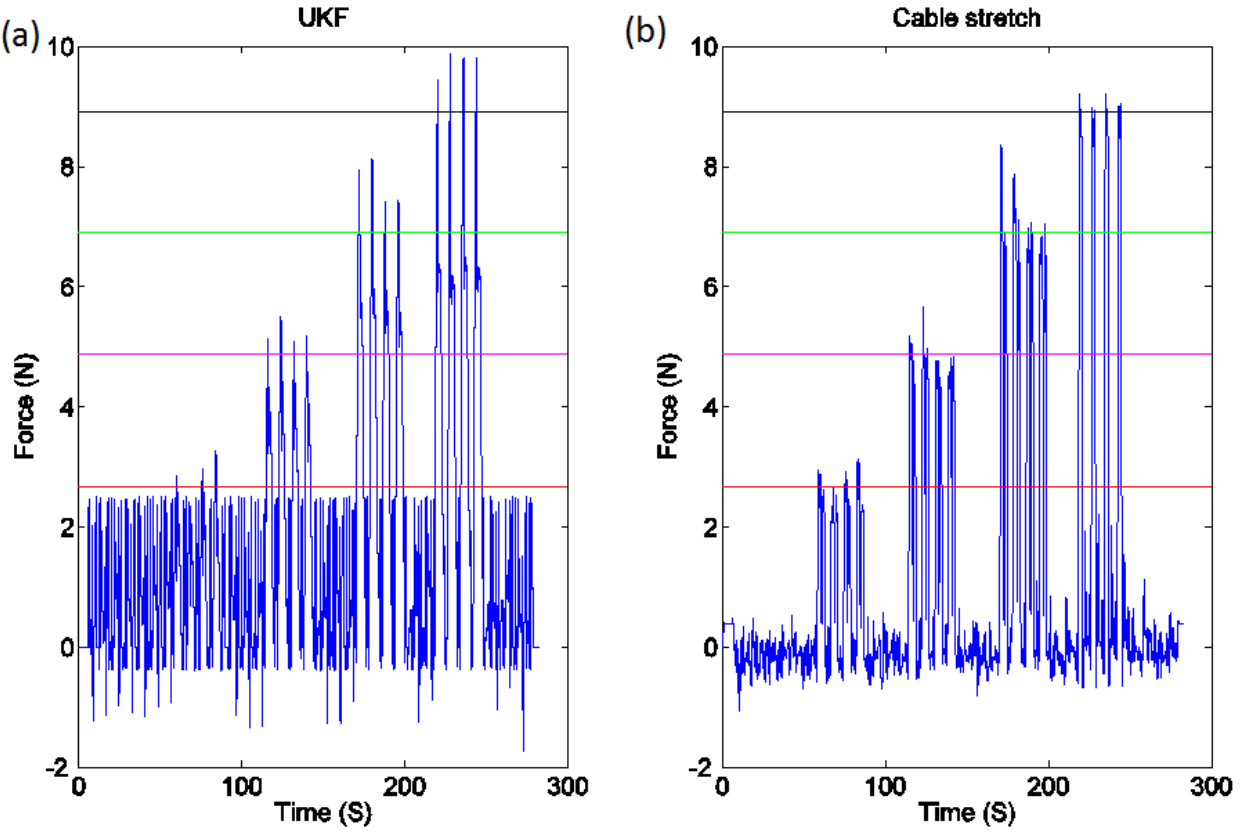

Figure 5.10: External Force estimation when lifting a basket up and down with (a) UKF method and (b) Cable stretch method. No load was applied on the first six cycles. Horizontal red, magenta, green, and black lines show the true values when 271g, 497g, 704g, and 910g weights were lifted respectively.

Experiment 3: Pulling Spring

After calibrating the force measurements for quadrants I & IV the robot was attached to a load cell sensor via a spring and a sinusoidal trajectory was performed to verify the proposed methods in quadrants I & IV. Load cell sensor data was used as a ground truth. Fig. 5.11 shows the force estimation and error histogram for both methods. From the results both methods provided force estimation close to the ground truth. The error histogram plot shows a higher error percentage is closer to zero in cable stretch method than UKF.

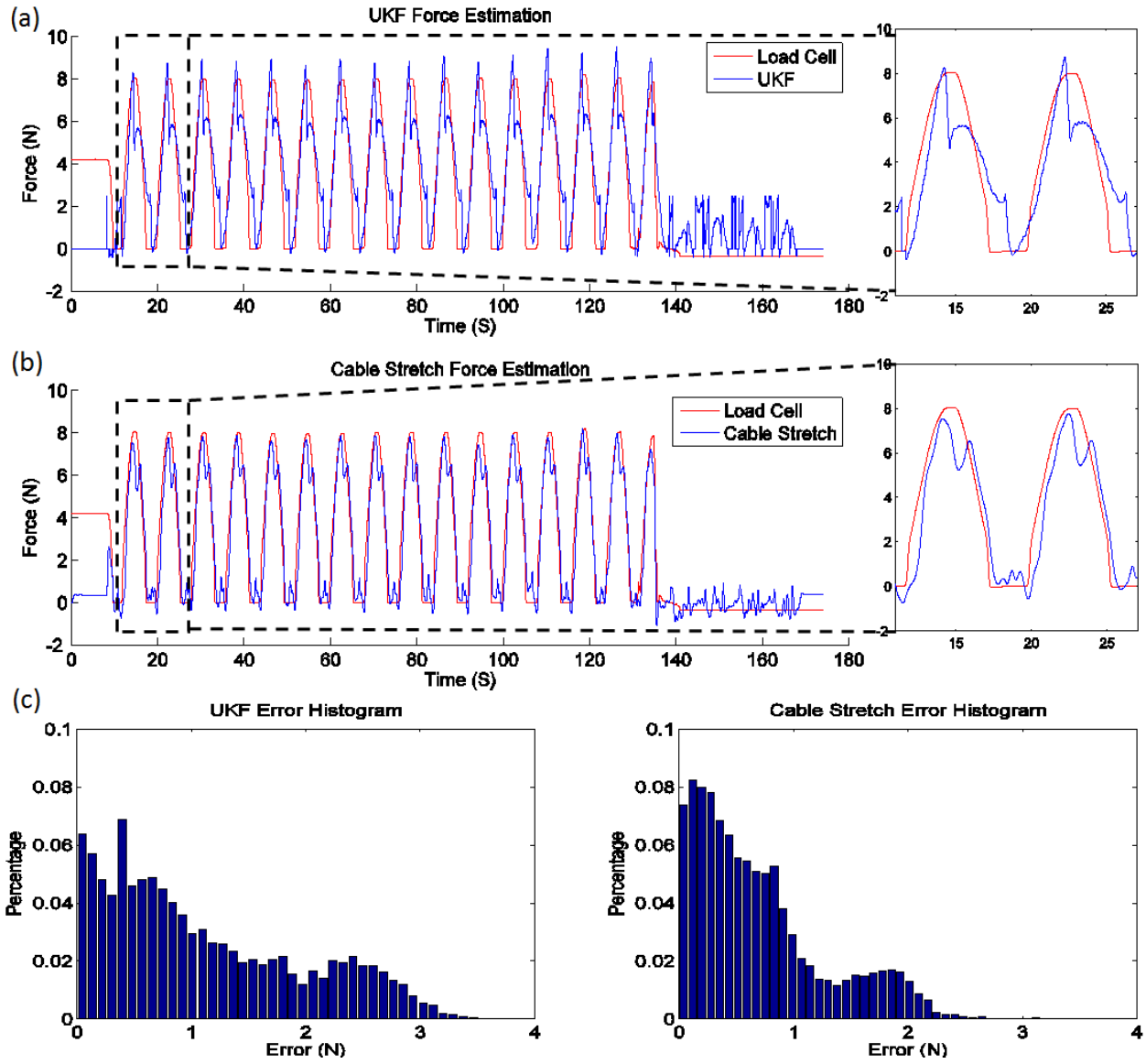

Figure 5.11: Force estimation on quadrants I and IV when pulling a spring in a sinusoidal motion. (a) External force estimation based on UKF method is plotted against load cell sensor measurements. (b) External force estimation based on cable stretch method is plotted against load cell sensor measurements. (c) Error histogram of UKF and cable stretch method.

Experiment 4: Pushing Spring

Lifting weights with the basket does not produce any force on quadrants II & III. Thus, to calibrate the force estimation for these quadrants a compression spring was attached to a load cell sensor and a sinusoidal trajectory was applied on the third link of the Raven-II to push the compressor spring. On the first half cycle of the sinusoidal trajectory the robot pushes the compression spring which generates force against the robot (quadrant III) while on the second half cycle of the sinusoidal trajectory, when the robot is moving up, the compression spring exerts force in the same direction as the robot motion (quadrant II). This experiment was repeated three times and each time the amplitude of the sinusoidal trajectory was changed. Changing the amplitude causes the robot to push the spring further which generates more force. The peak force value for each amplitude was used to calibrate the force estimation for quadrants II & III. Once the force estimation was calibrated, the experiment was repeated once more with a different sin trajectory amplitude to evaluate the performance of the force estimation. Fig. 5.12 shows the evaluation result for force estimation and error histogram utilizing both methods. From the plots, when external force is sufficiently large, both methods provided force estimation close to ground truth, however at lower forces, cable stretch method outperforms UKF method. This is consistent with the previous two experiments.

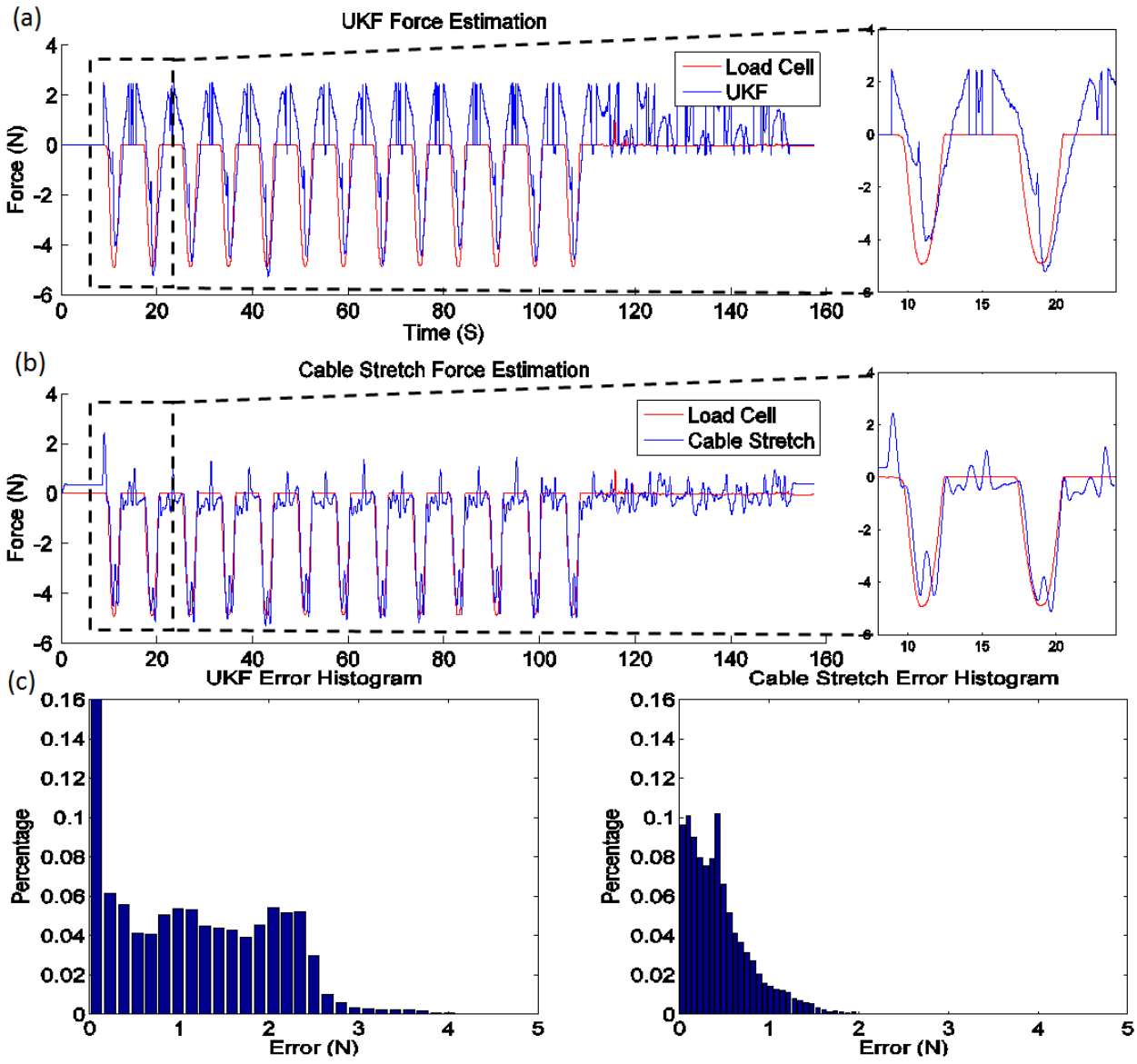

Figure 5.12: Force estimation on quadrants II and III when pushing a compressor spring in a sinusoidal motion. (a) External force estimation based on UKF method is plotted against load cell sensor measurements. (b) External force estimation based on cable stretch method is plotted against load cell sensor measurements. (c) Error histogram of UKF and cable stretch method.

Experiments 5 & 6: FLS Pushing & Pulling Spring

In addition to the sinusoidal trajectory, these methods were evaluated under a pre-recorded human-operator driven FLS trajectory. To cover the four quadrants, first a spring was attached between the load cell sensor and the robot while being pulled with FLS trajectory. Then a compression spring was attached between the load cell and robot while being pushed with the same FLS trajectory. The trajectory duration for both experiments was about 220 seconds. To observe the zero force estimation the spring was attached to the robot for the first 160s and 140s of the pull and push experiments, respectively. For the remaining duration of the trajectory the springs were detached from the robot. Fig. 5.13 and 5.14 shows the force estimation results and error histogram for both methods for pulling the spring (Quadrants I & IV) and pushing the spring (Quadrants II & III) respectively. The results of these experiments are also consistent with previous experiments.

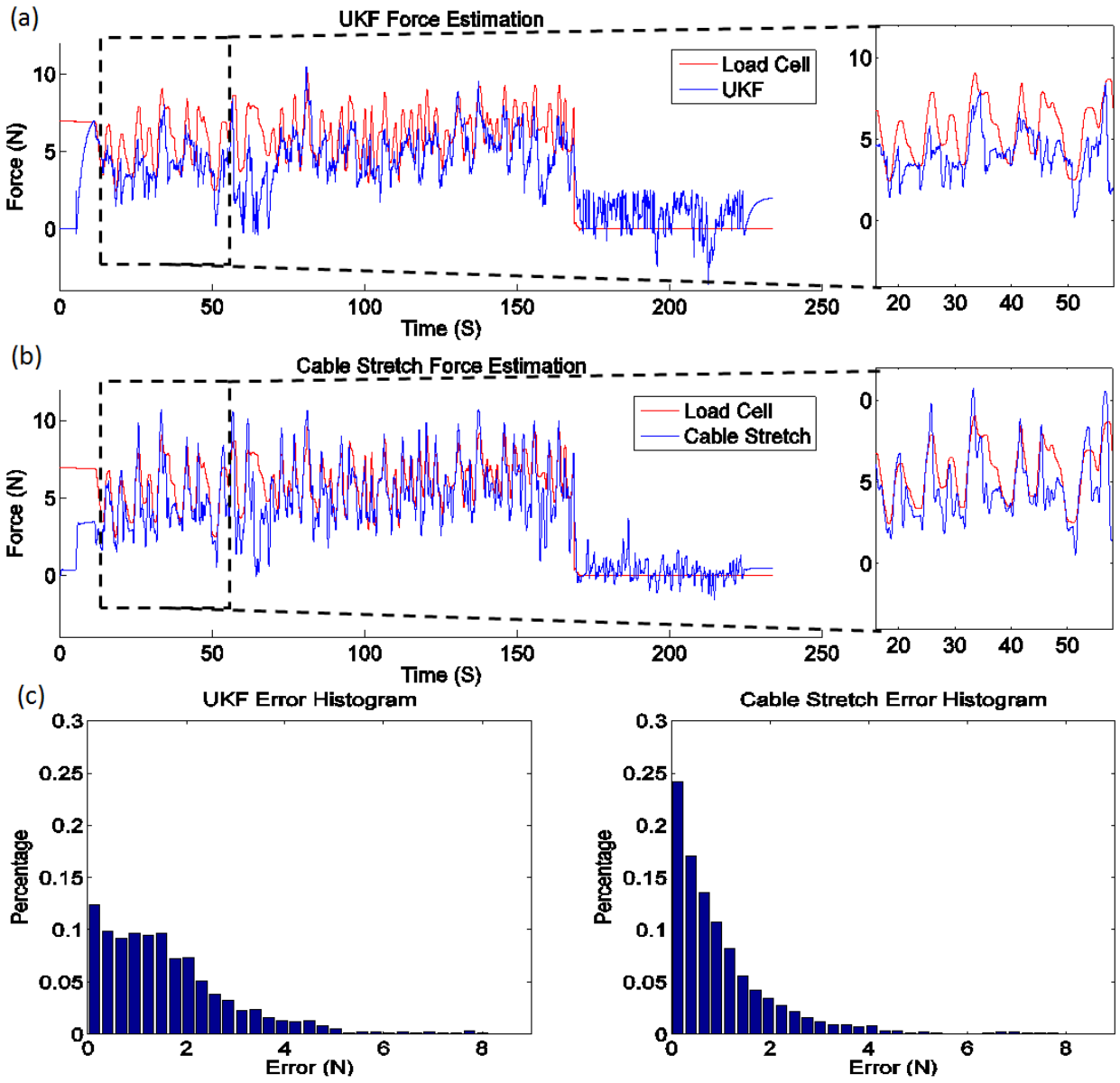

Figure 5.13: Force estimation on quadrants I and IV when pulling a spring with FLS trajectory. (a) External force estimation based on UKF method is plotted against load cell sensor measurements. (b) External force estimation based on cable stretch method is plotted against load cell sensor measurements. (c) Error histogram of UKF and cable stretch method.

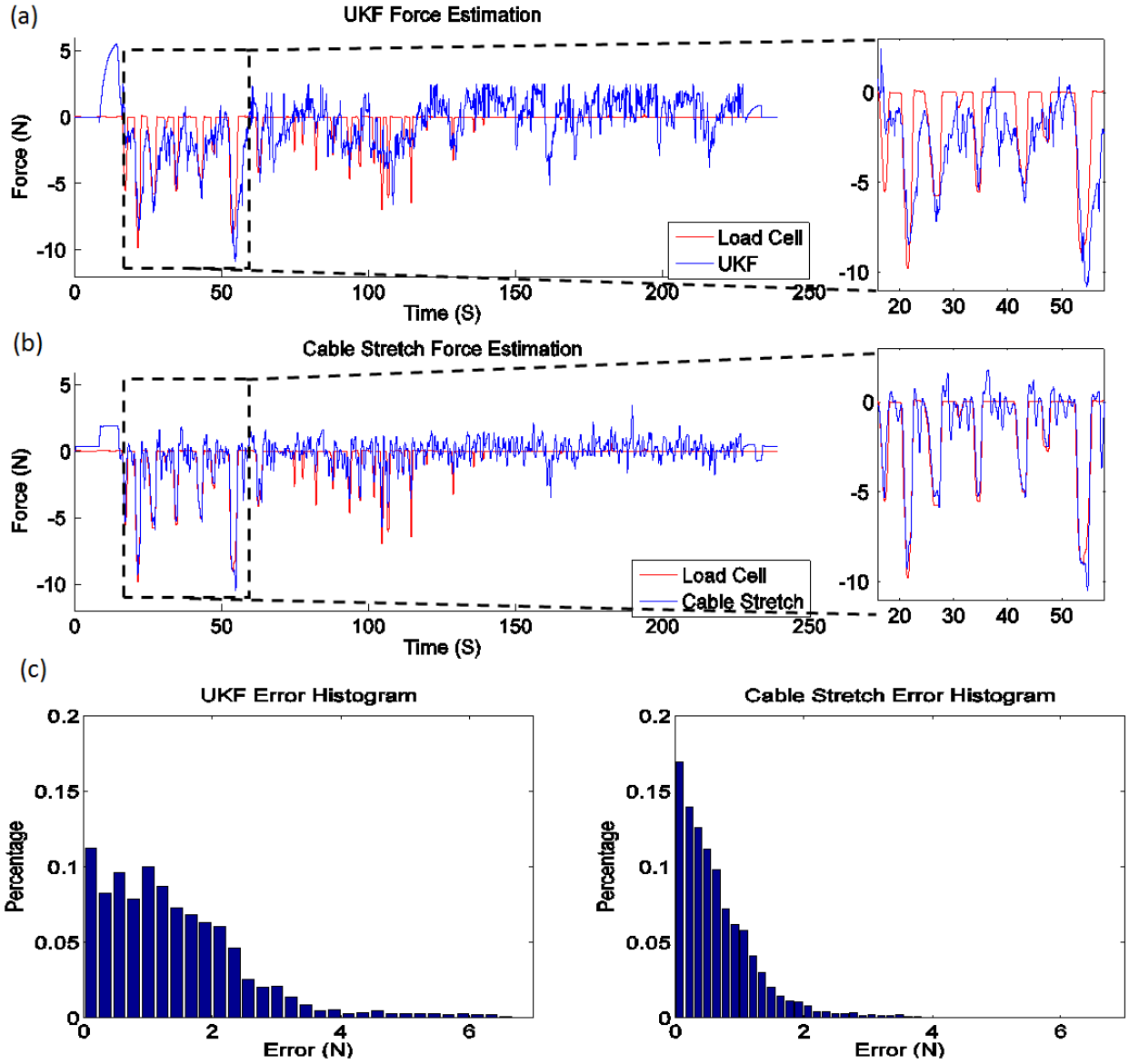

Figure 5.14: Force estimation on quadrants II and III when pushing a compressor spring with FLS trajectory. (a) External force estimation based on UKF method is plotted against load cell sensor measurements. (b) External force estimation based on cable stretch method is plotted against load cell sensor measurements. (c) Error histogram of UKF and cable stretch method.

The average errors, maximum errors, and standard deviations for experiments 3-6 are shown in Table 5.1. Based on the results, in all the experiments, the cable stretch method outperforms the UKF method observing motor torque only. With the cable stretch method, lower forces can be detected. Our results confirm that if the input torque is not large enough the stretch is not detectable by observing motor torque only as described in [64] , [65].

Table 5.1: Average, Max, and Standard Deviation error in Newton for both UKF and Cable Stretch methods.

Error (N)	Sin Pull		Sin Push		FLS Pull		FLS Push	
	UKF	*Cable Str.*	*UKF*	*Cable Str.*	*UKF*	*Cable Str.*	*UKF*	*Cable Str.*
Average	1.1006	0.6994	1.1052	0.4430	1.6011	1.2217	1.4006	0.6580
Max	3.5073	3.1583	4.5463	1.9720	8.1563	7.4347	6.6847	4.2728
SD	0.8521	0.5736	0.8803	0.3521	1.3152	1.0622	1.1153	0.5963

5.4 Conclusion

In this Chapter, a dynamic model based estimator was proposed to indirectly estimate the cable pre-tension in cable driven robots. Then, dynamic based estimators of [68] and [70] were further extended to estimate external forces in all the four quadrants. Moreover, for the case when joint encoder measurements are available, a cable stretch method was introduced and used to estimate external forces. The proposed methods were applied on the third link of Raven-II surgical research platform. By using dual UKF parameter and state estimation, system dynamics parameters F_c and K_e were tuned. By estimating K_e, cable pre-tension can indirectly be calculated with a mapping function that maps stiffness to tension. Furthermore, after estimating K_e and F_c, these values can be held constant to estimate F_{ex} online using dynamics and UKF with motor torque observation. We also evaluated a second approach to estimate external forces by taking advantage of cable elasticity similar to series elastic

actuators. The latter approach has less noise magnitude at lower forces as shown in Figs. 5.9 and 5.10; thus, it can provide better force estimation at lower forces. Moreover, in cable stretch method, precise optical encoders are being used to measure the stretch; whereas, in the UKF method, motor torque is indirectly measured from current for observation. Any uncertainty in dynamics and noise in motor torque may cause poor estimation.

Chapter 6
FUTURE OUTLOOK

This dissertation presented a method to improve the joint angle estimation in a serial cable driven manipulators by applying Unscented Kalman Filter and observing the end-effector with a set of stereo cameras. Furthermore, we proposed a method to indirectly estimate the cable pre-tension in these manipulators from cable's stiffness parameter. We also used the same technique to estimate external forces acting on the robot in all the four quadrants. We have also proposed estimating external forces by taking advantage of elasticity of cables similar to series elastic actuators. In this thesis, we tested the proposed methods on Raven-II which is a cable driven surgical robot experimental research platform. The joint angle estimations were tested on the first three degree of freedom of the Raven-II and the methods to estimate cable pre-tension and external force were applied on the third link of Raven-II.

Potential future work arising from this thesis will include extending these methods to other links of the Raven-II (even though their joints are coupled to multiple external force directions) by using its Jacobian matrix. Furthermore, by using the cable elasticity method, of Chapter 5 [72], compliance control can be integrated into cable driven robots. In surgery, this will help to prevent tissue damage by limiting excessive force exertion on tissues. Moreover, we plan to refine the robot dynamics by applying the models derived from experimental measurements presented in [73] and [74] and combine cable elasticity with UKF to further improve external force estimation on all the four quadrants.

BIBLIOGRAPHY

[1] G. Tholey, J. P. Desai, and A. E. Castellanos, "Force feedback plays a significant role in minimally invasive surgery: results and analysis," *Annals of surgery*, vol. 241, no. 1, pp. 102–109, 2005.

[2] E. Westebring-Van Der Putten, R. Goossens, J. Jakimowicz, and J. Dankelman, "Haptics in minimally invasive surgery-a review," *Minimally Invasive Therapy & Allied Technologies*, vol. 17, no. 1, pp. 3–16, 2008.

[3] G. Dogangil, B. Davies, and F. R. y Baena, "A review of medical robotics for minimally invasive soft tissue surgery," *Proceedings of the Institution of Mechanical Engineers, Part H: Journal of Engineering in Medicine*, vol. 224, no. 5, pp. 653–679, 2010.

[4] M. Tavakoli, *Haptics for teleoperated surgical robotic systems*, vol. 1. World Scientific, 2008.

[5] H. A. Tabaie, J. A. Reinbolt, W. P. Graper, T. F. Kelly, and M. A. Connor, "Endoscopic coronary artery bypass graft (e-cabg) procedure with robotic assistance," in *The heart surgery forum*, vol. 2, 1999.

[6] A. P. Kypson and W. R. Chitwood, "Robotic applications in cardiac surgery," *International Journal of Advanced Robotic Systems*, vol. 1, no. 2, p. 9, 2004.

[7] S. Dogan, T. Aybek, P. Risteski, S. Mierdl, H. Stein, C. Herzog, M. Khan, O. Dzemali, A. Moritz, and G. Wimmer-Greinecker, "Totally endoscopic coronary artery bypass graft: initial experience with an additional instrument arm and an advanced camera system," *Surgical Endoscopy and Other Interventional Techniques*, vol. 18, no. 11, pp. 1587–1591, 2004.

[8] B. A. Jones, S. Krueger, D. Howell, B. Meinecke, and S. Dunn, "Robotic mitral valve repair.," *Texas Heart Institute Journal*, vol. 32, no. 2, 2005.

[9] D. A. Murphy, J. S. Miller, D. A. Langford, and A. B. Snyder, "Endoscopic robotic mitral valve surgery," *The Journal of Thoracic and Cardiovascular Surgery*, vol. 132, no. 4, pp. 776–781, 2006.

[10] P. Puangmali, K. Althoefer, L. D. Seneviratne, D. Murphy, and P. Dasgupta, "State-of-the-art in force and tactile sensing for minimally invasive surgery," *IEEE Sensors Journal*, vol. 8, no. 4, pp. 371–381, 2008.

[11] B. Davies, "A review of robotics in surgery," *Proceedings of the Institution of Mechanical Engineers, Part H: Journal of Engineering in Medicine*, vol. 214, no. 1, pp. 129–140, 2000.

[12] G. Guthart and J. K. Salisbury Jr, "The intuitivetm telesurgery system: Overview and application.," in *ICRA*, pp. 618–621, 2000.

[13] B. Hannaford et al., "Raven-ii: an open platform for surgical robotics research," *Biomedical Engineering, IEEE Transactions on*, vol. 60, no. 4, pp. 954–959, 2013.

[14] J. Werkmeister and A. Slocum, "Theoretical and experimental determination of capstan drive stiffness," *precision Engineering*, vol. 31, no. 1, pp. 55–67, 2007.

[15] H.-C. Y. J.-J. Lee and M.-S. Chen, "Control for tendon-driven manipulators with flexible tendons using artificial potential field approach," in *12th IFToMM World Congress, Besançon, France*, Citeseer, 2007.

[16] O. Baser and E. I. Konukseven, "Theoretical and experimental determination of capstan drive slip error," *Mechanism and Machine Theory*, vol. 45, no. 6, pp. 815–827, 2010.

[17] S. Behzadipour and A. Khajepour, *Cable-based robot manipulators with translational degrees of freedom*. INTECH Open Access Publisher, 2006.

[18] S. N. Kosari, S. Ramadurai, H. J. Chizeck, and B. Hannaford, "Control and tension estimation of a cable driven mechanism under different tensions," in *International Design Engineering Technical Conferences and Computers and Information in Engineering Conference*, ASME, 2013.

[19] V. Pradeep, K. Konolige, and E. Berger, "Calibrating a multi-arm multi-sensor robot: A bundle adjustment approach," in *Experimental robotics*, pp. 211–225, Springer, 2014.

[20] H. Zhuang, K. Wang, and Z. S. Roth, "Simultaneous calibration of a robot and a hand-mounted camera," *IEEE Transactions on Robotics and Automation*, vol. 11, no. 5, pp. 649–660, 1995.

[21] B. Kehoe, G. Kahn, J. Mahler, J.-H. Kim, A. Lee, K. Nakagawa, S. Patil, W. D. Boyd, P. Abbeel, and K. Goldberg, "Autonomous multilateral debridement with the raven surgical robot," in *Robotics and Automation (ICRA), 2014 IEEE International Conference on*, pp. 1432–1439, IEEE, 2014.

[22] M. C. Readman, *Flexible joint robots*. CRC press, 1994.

[23] G. A. Pratt, M. M. Williamson, P. Dillworth, J. Pratt, and A. Wright, "Stiffness isn't everything," in *experimental robotics IV*, pp. 253–262, Springer, 1997.

[24] G. A. Pratt and M. M. Williamson, "Series elastic actuators," in *Intelligent Robots and Systems 95.'Human Robot Interaction and Cooperative Robots', Proceedings. 1995 IEEE/RSJ International Conference on*, vol. 1, pp. 399–406, IEEE, 1995.

[25] J. Austin, A. Schepelmann, and H. Geyer, "Control and evaluation of series elastic actuators with nonlinear rubber springs," in *Intelligent Robots and Systems (IROS), 2015 IEEE/RSJ International Conference on*, pp. 6563–6568, IEEE, 2015.

[26] D. W. Robinson, J. E. Pratt, D. J. Paluska, and G. A. Pratt, "Series elastic actuator development for a biomimetic walking robot," in *Advanced Intelligent Mechatronics,*

1999. Proceedings. 1999 IEEE/ASME International Conference on, pp. 561–568, IEEE, 1999.

[27] J. Hurst, A. Rizzi, and D. Hobbelen, "Series elastic actuation: Potential and pitfalls," in *International Conference on Climbing and Walking Robots*, 2004.

[28] J. W. Hurst, *The role and implementation of compliance in legged locomotion*. ProQuest, 2008.

[29] A. Seyfarth, H. Geyer, R. Blickhan, S. Lipfert, J. Rummel, Y. Minekawa, and F. Iida, "Running and walking with compliant legs," in *Fast motions in biomechanics and robotics*, pp. 383–401, Springer, 2006.

[30] S. Ford, D. Rollinson, A. Willig, and H. Choset, "Online calibration of a compact series elastic actuator," in *American Control Conference (ACC), 2014*, pp. 3329–3334, IEEE, 2014.

[31] S. Thrun, W. Burgard, and D. Fox, *Probabilistic robotics*. MIT press, 2005.

[32] Y. Bar-Shalom, X. R. Li, and T. Kirubarajan, *Estimation with applications to tracking and navigation: theory algorithms and software*. John Wiley & Sons, 2004.

[33] C. Dunis, S. Likothanassis, A. Karathanasopoulos, G. Sermpinis, and K. Theofilatos, *Computational Intelligence Techniques for Trading and Investment*. Routledge, 2014.

[34] S. J. Julier and J. K. Uhlmann, "A new extension of the kalman filter to nonlinear systems," in *Int. symp. aerospace/defense sensing, simul. and controls*, vol. 3, pp. 3–2, Orlando, FL, 1997.

[35] S. J. Julier and J. Uhlmann, "A general method for approximating nonlinear transformations of probability distributions," tech. rep., Technical report, Robotics Research Group, Department of Engineering Science, University of Oxford, 1996.

[36] W. Khalil and E. Dombre, *Modeling, identification and control of robots*. Butterworth-Heinemann, 2004.

[37] S. Ramadurai et al., "Application of unscented kalman filter to a cable driven surgical robot: A simulation study," in *Robotics and Automation (ICRA), International Conference on*, pp. 1495–1500, IEEE, 2012.

[38] E. Naerum, H. H. King, and B. Hannaford, "Robustness of the unscented kalman filter for state and parameter estimation in an elastic transmission.," in *Robotics: Science and Systems*, Citeseer, 2009.

[39] J. J. Craig, *Introduction to robotics: mechanics and control*, vol. 3. Pearson Prentice Hall Upper Saddle River, 2005.

[40] R. Van Der Merwe and E. A. Wan, "The square-root unscented kalman filter for state and parameter-estimation," in *Acoustics, Speech, and Signal Processing (ICASSP'01). International Conference on*, vol. 6, pp. 3461–3464, IEEE, 2001.

[41] A. H. Sayed and T. Kailath, "A state-space approach to adaptive rls filtering," *Signal Processing Magazine, IEEE*, vol. 11, no. 3, pp. 18–60, 1994.

[42] E. A. Wan and R. Van Der Merwe, "The unscented kalman filter for nonlinear estimation," in *Adaptive Systems for Signal Processing, Communications, and Control Symposium. AS-SPCC*, pp. 153–158, IEEE, 2000.

[43] J. Gove and D. Hollinger, "Application of a dual unscented kalman filter for simultaneous state and parameter estimation in problems of surface-atmosphere exchange," *Journal of Geophysical Research: Atmospheres (1984–2012)*, vol. 111, no. D8, 2006.

[44] S. S. Haykin, S. S. Haykin, and S. S. Haykin, *Kalman filtering and neural networks*. Wiley Online Library, 2001.

[45] M. Quigley et al., "Ros: an open-source robot operating system," in *ICRA workshop on open source software*, vol. 3, p. 5, 2009.

[46] W. T. Vetterling, S. A. Teukolsky, and W. H. Press, *Numerical recipes: example book (C)*. Press Syndicate of the University of Cambridge, 1992.

[47] G. M. Fried, "Fls assessment of competency using simulated laparoscopic tasks," *Journal of Gastrointestinal Surgery*, vol. 12, no. 2, pp. 210–212, 2008.

[48] A. Reiter, P. K. Allen, and T. Zhao, "Appearance learning for 3d tracking of robotic surgical tools," *The International Journal of Robotics Research*, vol. 33, no. 2, pp. 342–356, 2014.

[49] C. E. Attinger, E. Bulan, and P. A. Blume, "Surgical debridement. the key to successful wound healing and reconstruction.," *Clinics in podiatric medicine and surgery*, vol. 17, no. 4, pp. 599–630, 2000.

[50] M. Granick, J. Boykin, R. Gamelli, G. Schultz, and M. Tenenhaus, "Toward a common language: surgical wound bed preparation and debridement," *Wound repair and regeneration*, vol. 14, no. s1, pp. S1–S10, 2006.

[51] J. Mahler, S. Krishnan, M. Laskey, S. Sen, A. Murali, B. Kehoe, S. Patil, J. Wang, M. Franklin, P. Abbeel, *et al.*, "Learning accurate kinematic control of cable-driven surgical robots using data cleaning and gaussian process regression," in *Automation Science and Engineering (CASE), 2014 IEEE International Conference on*, pp. 532–539, IEEE, 2014.

[52] C. E. Rasmussen, "Gaussian processes for machine learning," 2006.

[53] J. M. Wang, D. J. Fleet, and A. Hertzmann, "Gaussian process dynamical models," in *NIPS*, vol. 18, p. 3, 2005.

[54] B. Hannaford, J. Ma, H. King, and S. Kosari, "Kinematic analysis of the ravenii(tm) research surgical robot platform," tech. rep., Department of Electrical Engineering, University of Washington, 2012.

[55] G. Bradski and A. Kaehler, *Learning OpenCV: Computer vision with the OpenCV library.* " O'Reilly Media, Inc.", 2008.

[56] J. Rosen, B. Hannaford, and R. M. Satava, *Surgical Robotics: Systems Applications and Visions.* Springer Science & Business Media, 2011.

[57] R. Christopher, S. Nicholas, and D. Robert, "The role of force feedback in surgery: analysis of blunt dissection," in *10th symposium on haptic interface for virtual environment and teleoperator systems*, vol. 1, pp. 18–125, Orlando: IEEE Computer Society, 2002.

[58] P. Puangmali, H. Liu, L. D. Seneviratne, P. Dasgupta, and K. Althoefer, "Miniature 3-axis distal force sensor for minimally invasive surgical palpation," *Ieee/Asme Transactions On Mechatronics*, vol. 17, no. 4, pp. 646–656, 2012.

[59] T. Ohtsuka, A. Furuse, T. Kohno, J. Nakajima, K. Yagyu, and S. Omata, "Application of a new tactile sensor to thoracoscopic surgery: experimental and clinical study," *The Annals of thoracic surgery*, vol. 60, no. 3, pp. 610–614, 1995.

[60] D. P. Noonan, H. Liu, Y. H. Zweiri, K. A. Althoefer, and L. D. Seneviratne, "A dual-function wheeled probe for tissue viscoelastic property identification during minimally invasive surgery," in *Robotics and Automation, 2007 IEEE International Conference on*, pp. 2629–2634, IEEE, 2007.

[61] A. L. Trejos, J. Jayender, M. Perri, M. D. Naish, R. V. Patel, and R. Malthaner, "Robot-assisted tactile sensing for minimally invasive tumor localization," *The International Journal of Robotics Research*, vol. 28, no. 9, pp. 1118–1133, 2009.

[62] T. Yamamoto, B. Vagvolgyi, K. Balaji, L. L. Whitcomb, and A. M. Okamura, "Tissue property estimation and graphical display for teleoperated robot-assisted surgery," in

Robotics and Automation, 2009. ICRA'09. IEEE International Conference on, pp. 4239–4245, IEEE, 2009.

[63] H. Liu, D. P. Noonan, B. J. Challacombe, P. Dasgupta, L. D. Seneviratne, and K. Althoefer, "Rolling mechanical imaging for tissue abnormality localization during minimally invasive surgery," *IEEE Transactions on Biomedical Engineering*, vol. 57, no. 2, pp. 404–414, 2010.

[64] F. Anooshahpour, I. G. Polushin, and R. V. Patel, "Quasi-static modeling of the da vinci instrument," in *2014 IEEE/RSJ International Conference on Intelligent Robots and Systems*, pp. 1308–1313, IEEE, 2014.

[65] F. Anooshahpour, I. G. Polushin, and R. V. Patel, "Tissue compliance determination using a da vinci instrument," in *2015 IEEE International Conference on Robotics and Automation (ICRA)*, pp. 5344–5349, IEEE, 2015.

[66] A. Faragasso, J. Bimbo, Y. Noh, A. Jiang, S. Sareh, H. Liu, T. Nanayakkara, H. A. Wurdemann, and K. Althoefer, "Novel uniaxial force sensor based on visual information for minimally invasive surgery," in *2014 IEEE International Conference on Robotics and Automation (ICRA)*, pp. 1405–1410, IEEE, 2014.

[67] J. Rosen, B. Hannaford, M. P. MacFarlane, and M. N. Sinanan, "Force controlled and teleoperated endoscopic grasper for minimally invasive surgery-experimental performance evaluation," *IEEE Transactions on Biomedical Engineering*, vol. 46, no. 10, pp. 1212–1221, 1999.

[68] S. N. Kosari, S. Ramadurai, H. J. Chizeck, and B. Hannaford, "Robotic compression of soft tissue," in *Robotics and Automation (ICRA), 2012 IEEE International Conference on*, pp. 4654–4659, IEEE, 2012.

[69] M. Haghighipanah, Y. Li, M. Miyasaka, and B. Hannaford, "Improving position precision of a servo-controlled elastic cable driven surgical robot using unscented kalman

filter," in *Intelligent Robots and Systems (IROS), 2015 IEEE International Conference on*, IEEE, 2015.

[70] Y. Li, M. Miyasaka, M. Haghighipanah, L. Cheng, and B. Hannaford, "Dynamic modeling of cable driven elongated surgical instruments for sensorless grip force estimation," in *2016 IEEE International Conference on Robotics and Automation (ICRA)*, pp. 4128–4134, IEEE, 2016.

[71] M. Haghighipanah, M. Miyasaka, Y. Li, and B. Hannaford, "Unscented kalman filter and 3d vision to improve cable driven surgical robot joint angle estimation," in *2016 IEEE International Conference on Robotics and Automation (ICRA)*, pp. 4135–4142, IEEE, 2016.

[72] M. Haghighipanah, M. Miyasaka, and B. Hannaford, "Utilizing elasticity of cable driven surgical robot to estimate cable tension and external force," *IEEE Robotics and Automation Letters*, 2017.

[73] M. Miyasaka, J. Matheson, A. Lewis, and B. Hannaford, "Measurement of the cable-pulley coulomb and viscous friction for a cable-driven surgical robotic system," in *Intelligent Robots and Systems (IROS), 2015 IEEE/RSJ International Conference on*, pp. 804–810, IEEE, 2015.

[74] M. Miyasaka, M. Haghighipanah, Y. Li, and B. Hannaford, "Hysteresis model of longitudinally loaded cable for cable driven robots and identification of the parameters," in *Robotics and Automation (ICRA), 2016 IEEE International Conference on*, pp. 4051–4057, IEEE, 2016.

VITA

Mohammad Haghighipanah earned his Bachelor of Science in Electrical Engineering from University of Washington (UW) in 2008. He received a certificate in Embedded and Real-Time System Programming in 2011. He then joined the BioRobotics Laboratory at UW in 2012 and started pursuing his Ph.D. in Electrical Engineering under the supervision of Professor Blake Hannaford. While pursuing his Ph.D., he also received Master of Science in Electrical Engineering in 2014. During his Ph.D., he has worked on Raven-II surgical robot platform and investigated methods to improve the positioning accuracy and estimating external forces on cable driven robots. Mohammad is an IEEE student member and has peer reviewed papers in International Conference on Robotics and Automation (ICRA).